UNIVERSIDAD DE CONCEPCIÓN
FACULTAD DE CIENCIAS FÍSICAS Y MATEMÁTICAS

Simulaciones NBODY de la formación de objetos masivos centrales en sistemas estelares densos bajo rotación (Direct N-body simulations of central massive object formation in rotating dense stellar systems)

Por: Fernando Cuevas Fuentealba

Tesis presentada a la Facultad de Ciencias Físicas y Matemáticas de la Universidad de Concepción para optar al grado académico de Magíster en Astronomía

Diciembre 2025
Concepción, Chile

Profesores Guía: Dominik Schleicher
& Nathan Leigh

ACKNOWLEDGMENTS

I would first like to express my deepest gratitude to my advisors, Dominik Schleicher and Nathan Leigh. I am truly thankful to them not only for their invaluable guidance but also for all the opportunities they have given me throughout the program. Thanks to their support, I was able to continue and complete this journey.

I am also deeply grateful to Marcelo C. Vergara and Francesco Flammini Dotti for their mentorship, support, and advice. Their help was crucial for my work; without it, I would not have been able to make such progress.

I would like to thank my family and friends, who stood by my side through good and difficult times, and whose constant support has meant everything to me. I also wish to acknowledge all of my cats — Grillo, Gloria, Garfield, Trinidad, Piolín, Canario, Marcelo and his cat Waton Rorschach, as well as my cats Waren and Venecia — for their companionship along the way.

I am sincerely thankful to the Heidelberg research group for their warm welcome, for the guidance and the insight they offered me in 2023.

I would also like to express my appreciation to 冨樫 義博. Although it may seem like a small thing, his work has inspired and motivated me since childhood to grow as a person and to keep pushing forward.

At last I gratefully acknowledge the financial support that made possible this work, provided by the Centro de Excelencia en Astrofisica y Tecnologias Afines (CATA) through the BASAL project FB210003, and by the Nucleo Milenio TITANS through the project NCN19-058.

Resumen

Los cúmulos estelares densos evolucionan mediante procesos de relajación a largo plazo donde los encuentros de dos cuerpos determinan su estructura. En sistemas compactos, el enfoque gravitacional incrementa la probabilidad de colisiones estelares, lo que puede conducir a un crecimiento desbocado y a la formación de un objeto masivo central. Esta tesis estudia la evolución dinámica temprana de cúmulos densos en el régimen colisional mediante simulaciones directas de N-cuerpos con NBODY6++GPU, enfocándose en la contracción del núcleo, las colisiones estelares y las condiciones para la formación de agujeros negros masivos.

Los modelos de cúmulos de masa igual basados en configuraciones de King con distintas concentraciones iniciales ($W_0 = 2$–12) y rotaciones ($\omega_0 = 0.0$–1.8) muestran que la concentración es el factor principal en la contracción y la actividad colisional temprana, mientras que la rotación acelera estos procesos. La actividad colisional alcanza su máximo cerca del colapso del núcleo y disminuye posteriormente por efecto de la evolución estelar. Estos resultados respaldan el papel de los cúmulos densos como posibles escenarios de formación de semillas de agujeros negros masivos e intermedios, sensibles a la estructura, rotación y evolución estelar.

Keywords – agujeros negros: formacion – estrellas: agujeros negros – metodos: numéricos – teoría

Abstract

Dense stellar clusters evolve through long-term relaxation processes where two-body encounters shape their structure. In compact systems, gravitational focusing increases the likelihood of stellar collisions, potentially leading to runaway growth and the formation of a massive central object. This thesis explores the early dynamical evolution of dense clusters in the collisional regime using direct N-body simulations with NBODY6++GPU, focusing on core contraction, stellar collisions, and conditions for massive black hole formation.

Models of equal-mass King clusters with varying initial concentration ($W_0 = 2$–12) and rotation ($\omega_0 = 0.0$–1.8) reveal that concentration primarily drives early core collapse and collision rates, while rotation accelerates these processes. Collisional activity peaks near core collapse and is limited at later stages by stellar evolution. These results support dense clusters as potential sites for the formation of massive and intermediate-mass black hole seeds, sensitive to structure, rotation, and stellar evolution

Keywords – black hole formation – stars: black hole – methods: numerical – theory

Contents

List of Tables

List of Figures

Chapter 1

Introduction

Black holes (BHs) are astrophysical objects characterized by their extreme densities, capable of bending and trapping light as predicted by the solutions of general relativity, and represent the densest known objects in the universe. There are various ways to classify BHs according to their properties; a common criterion is to distinguish them by mass, disregarding spin and charge. The smallest and most speculative class are the *primordial black holes* (PBHs), which are hypothesized to have formed in the early Universe from the direct collapse of high-density fluctuations shortly after the Big Bang, rather than from stellar evolution (Carr and Hawking, 1974; Hawking, 1971). Their existence remains unconfirmed, but they are of cosmological interest as potential dark matter candidates.

Excluding the primordial population, the smallest BHs known to form through astrophysical processes are the stellar black holes (SBHs), which, as their name implies, originate from the collapse of sufficiently massive stars ($m_\star > 20\,M_\odot$) and typically have masses from a few solar masses up to $\sim 150\,M_\odot$. Intermediate-mass black holes (IMBHs) are expected to occupy the range $\sim 150\,M_\odot$ to $10^6\,M_\odot$, while those exceeding $10^6\,M_\odot$ are classified as supermassive black holes (SMBHs), commonly found at the centers of nearby galaxies (Schneider et al., 2002; Heger et al., 2003; Volonteri, 2010; Mezcua, 2017; Barack et al., 2019; Abbott et al., 2020).

Even though BHs have been studied over the course of the last century, there is still no definitive and clear answer to explain the origin and early growth of the most massive ones (Volonteri et al., 2021). Observationally, the properties of host

galaxies are tightly correlated with those of their central SMBHs (Ferrarese and Merritt, 2000; Gebhardt et al., 2000; Häring and Rix, 2004; Volonteri, 2010; Leigh et al., 2012; Reines and Volonteri, 2015; Nguyen et al., 2018; Barack et al., 2019).

The empirical correlation between the mass of supermassive black holes and the stellar velocity dispersion of their host bulges—the so-called $M_{\rm BH}$–σ relation—can be traced back to seminal investigations such as Ferrarese and Merritt (2000) and Gebhardt et al. (2000), which first quantified this connection and established it as a cornerstone of galaxy–black hole coevolution studies. Figure 1.0.1 illustrates how the black hole mass scales with the central stellar velocity dispersion, revealing a tight, nearly power-law correlation across elliptical galaxies and bulges, with remarkably small intrinsic scatter.

The existence and tightness of the $M_{\rm BH}$–σ relation strongly suggest that the growth of central black holes is intimately linked to the dynamical state of their surrounding stellar systems. Although the relation is observed on galactic scales, it provides key motivation for investigating the physical processes that regulate black hole formation and growth in dense stellar environments more generally. In particular, it raises the question of whether similar dynamical mechanisms—such as relaxation-driven contraction and runaway stellar collisions—may operate at earlier cosmic times and on smaller spatial scales, potentially giving rise to massive black hole seeds in dense star clusters.

Subsequent work extended these correlations to other global galaxy properties, most notably the total stellar mass of the host galaxy (Reines and Volonteri, 2015). Figure 1.0.2 shows the empirical relation between black hole mass and total stellar mass for both active and inactive galaxies, spanning several orders of magnitude in $m_\star$. In contrast to the $M_{\rm BH}$–σ relation, which links black hole mass to the dynamical state of the stellar system, this scaling highlights a close connection between black hole growth and the overall build-up of stellar mass.

The approximately linear trend observed in Figure 1.0.2, together with its persistence across galaxy types and activity levels, suggests that black hole mass assembly proceeds in tandem with galaxy growth over a wide range of masses. The extension of this relation to lower-mass is particularly relevant in the context of black hole seeding, as it implies that the physical processes governing black hole formation and early growth must already be effective in massive, and therefore

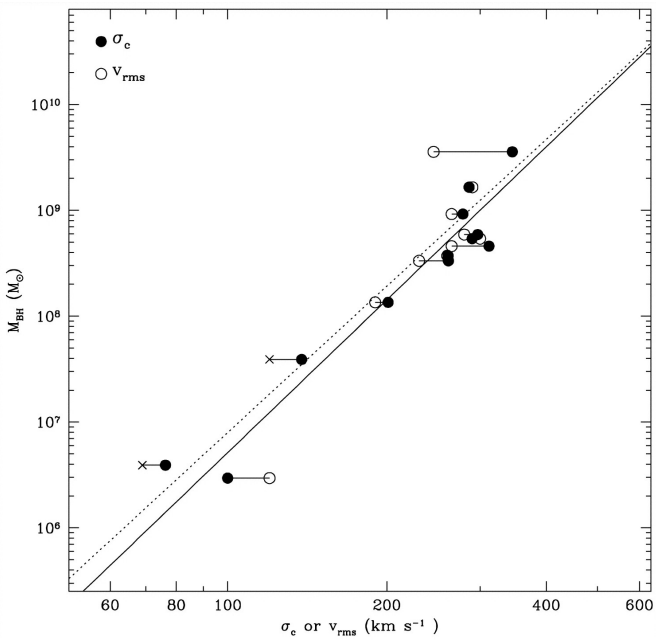

Figure 1.0.1: Empirical relation between black hole mass and the central velocity dispersion (σ_c) of the host galaxy bulge or elliptical galaxy. Filled circles correspond to σ_c; open circles denote the rms velocity $v_{\rm rms}$ measured at one-fourth of the effective radius, while crosses represent lower limits in $v_{\rm rms}$. The solid and dashed lines indicate the best-fit linear relations using σ_c and $v_{\rm rms}$, respectively. Reproduced from Ferrarese and Merritt (2000), Figure 2, *The Astrophysical Journal Letters*, 539, L9, © 2000 The American Astronomical Society.

rapidly evolving stellar environments. These empirical findings provide strong motivation for exploring cluster-scale formation channels for massive black hole seeds, as investigated in this thesis.

1.1 Black hole formation channels

While the formation of stellar-mass black holes (SBHs) is relatively well understood as the endpoint of massive stellar evolution (Heger et al., 2003), the origin of more massive black holes remains an open problem. In particular, the formation pathways of intermediate-mass black holes (IMBHs), which are expected to bridge the gap between SBHs and supermassive black holes (SMBHs), are still actively debated. Current theoretical frameworks generally describe SMBHs as the result of the growth of smaller black hole seeds through gas accretion and mergers; however, the nature and origin of these initial seeds remain uncertain (Volonteri, 2010; Barack et al., 2019; Volonteri et al., 2021).

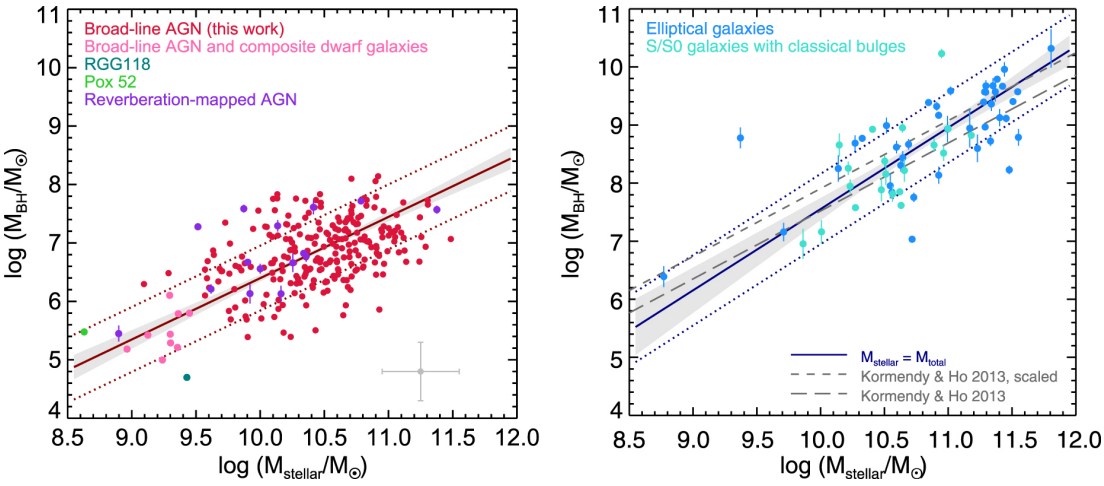

Figure 1.0.2: Relation between black hole mass and total stellar mass for local galaxies. (*Left*) Active galaxies (AGNs), showing the best-fit $M_{\rm BH}$–$m_\star$ relation (dark red line) with the shaded region indicating uncertainties in slope and intercept, and dotted lines denoting the rms scatter. (*Right*) Same relation for inactive galaxies, divided by morphological type, as described in Section 3.3 of the original publication. Reproduced from Reines and Volonteri (2015), Figure 10, *The Astrophysical Journal*, 813, 82, © 2015 The American Astronomical Society.

Several channels have been proposed for the formation of the first black hole seeds. One possibility involves the remnants of the first generation of stars formed at high redshift, commonly referred to as Population III (Pop III) stars. Owing to their low metallicity and inefficient cooling, Pop III stars are predicted to form with a top-heavy initial mass function, producing very massive stellar remnants capable of collapsing directly into black holes (Schneider et al., 2002; Heger et al., 2003; Bromm and Larson, 2004).

Alternative scenarios invoke the direct collapse of primordial gas in early proto-galaxies, forming massive black hole seeds ($M_\bullet \sim 10^{5\text{–}6}\,M_\odot$) without an intermediate stellar phase. Such gas-dominated channels, while promising, require specific environmental conditions—such as strong Lyman–Werner radiation fields or rapid halo mergers—and remain subject to large theoretical uncertainties.

A third, dynamically driven pathway arises in dense stellar systems (Portegies Zwart et al., 1999; Portegies Zwart and McMillan, 2002; Glebbeek et al., 2009, 2013; Reinoso et al., 2018; Alister Seguel et al., 2020; Reinoso et al., 2020; Escala, 2021; Das et al., 2021; Vergara et al., 2022; Sehlke-Abarca et al., 2023; Vergara et al., 2025; Escala et al., 2025). In globular clusters (GCs), nuclear star clusters (NSCs), or young massive clusters, high stellar densities and short relaxation

times favor rapid mass segregation, core collapse, and frequent stellar collisions. Runaway collisional growth can then produce a very massive merger product that subsequently collapses into an IMBH. This process is purely stellar-dynamical and largely independent of gas accretion, with its efficiency primarily governed by cluster properties such as concentration and rotation.

The main black hole seed-formation channels discussed above are summarized schematically in Figure 1.1.1. The figure illustrates the wide range of physical environments and initial temperatures and mass scales associated with proposed formation pathways, spanning several orders of magnitude from stellar-mass remnants of Population III stars to massive seeds formed via direct gas collapse in atomic-cooling halos. These scenarios can be broadly divided into gas-dynamical channels, which rely on the suppression of fragmentation and rapid inflow, and stellar-dynamical channels, which operate in extremely dense stellar systems.

Of particular relevance for this work is the channel involving runaway stellar collisions in ultra-dense clusters (pathway 3 in Figure 1.1.1), which can lead to the formation of very massive stars and subsequently massive black hole seeds with masses of $\sim 10^3$–$10^4\,M_\odot$. Unlike direct-collapse models, this pathway does not require fine-tuned thermodynamical conditions, but instead depends sensitively on the internal dynamical evolution of the cluster, including relaxation-driven core contraction and high stellar collision rates. As such, Figure 1.1.1 provides the broader theoretical context within which the present thesis investigates dense stellar clusters as viable sites for massive black hole seed formation.

Recent observations with the *James Webb Space Telescope* (JWST) have begun to reveal potential analogs of seed-forming environments at very high redshift. A particularly remarkable example is the galaxy system known as *Firefly Sparkle*, observed at $z \approx 8.3$, corresponding to an age of roughly 600 Myr after the Big Bang (Figure 1.3.1). Within this young system, Mowla et al. (2024) identified approximately ten compact stellar clusters with individual masses of 10^5–$10^6\,M_\odot$ and a combined stellar mass of $\sim 10^7\,M_\odot$. These clusters exhibit exceptionally high surface mass densities ($> 10^3\,M_\odot\,\mathrm{pc}^{-2}$), indicative of extremely dense stellar environments, suggestive of a top-heavy initial mass function.

Such conditions are broadly consistent with those required for runaway stellar collisions and the formation of very massive stars, as envisioned in the stellar-

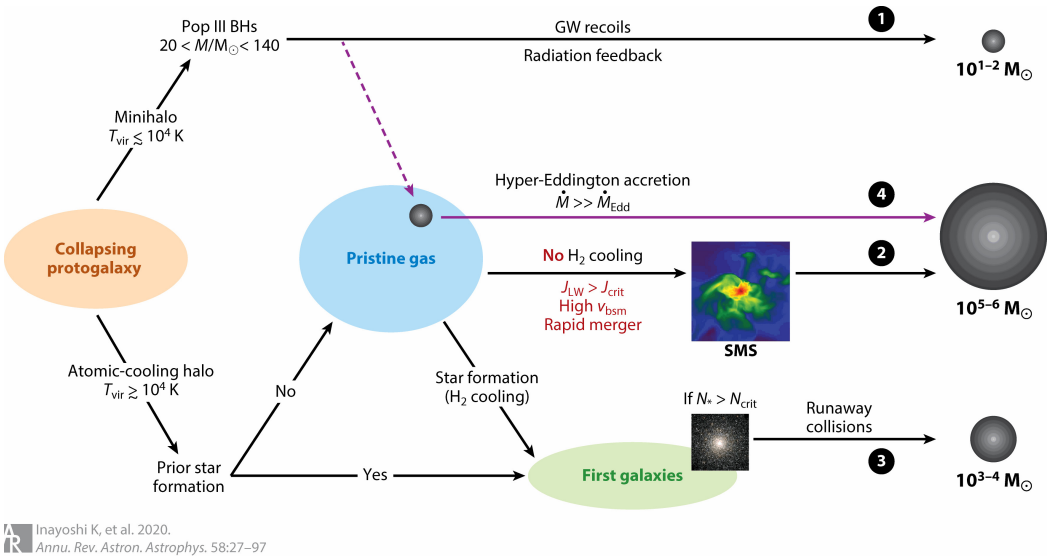

Figure 1.1.1: Schematic overview of the main theoretical channels proposed for the formation of massive black hole seeds in the early Universe. (1) Remnants of Population III stars ($M_\bullet \sim 10^{1-2}\,M_\odot$); (2) direct-collapse black holes forming in atomic-cooling halos under extreme conditions ($M_\bullet \sim 10^{5-6}\,M_\odot$); (3) runaway stellar collisions in ultra-dense clusters leading to very massive stars ($M_\bullet \sim 10^{3-4}\,M_\odot$); and (4) hyper-Eddington accretion onto stellar-mass black holes. Reproduced from Inayoshi, K., Visbal, E., & Haiman, Z. (2020), *Annual Review of Astronomy and Astrophysics*, 58, 27–97, © 2020 Annual Reviews. All rights reserved.

dynamical black hole seed formation channel discussed above. The *Firefly Sparkle* system therefore provides a compelling observational motivation for investigating dense star clusters as potential sites for the formation of massive and intermediate-mass black hole seeds in the early Universe.

1.2 Black holes in dense stellar clusters

This work focuses on the collisional formation pathway, and therefore requires identifying astrophysical environments in which stellar collisions can efficiently drive the growth of black holes to seed-mass scales. Among the most promising candidates are nuclear star clusters (NSCs), which are the densest stellar systems observed in the Universe. NSCs are characterized by effective radii of order ~ 5 pc, surface mass densities reaching $\sim 10^6\,M_\odot\,\mathrm{pc}^{-2}$, and central volumetric densities on sub-parsec scales as high as $10^7\,M_\odot\,\mathrm{pc}^{-3}$ (Neumayer et al., 2020).

Such extreme stellar densities naturally enhance the frequency of close encounters

and physical collisions, making NSCs favorable environments for runaway stellar growth and repeated merger events. In addition, NSCs are commonly found at the dynamical centers of galaxies, coexisting with central SMBH (Georgiev et al., 2016). While this spatial association does not by itself establish a causal connection, it motivates the hypothesis that dense stellar clusters may play a key role in the early stages of massive black hole assembly.

In this context, dense star clusters provide a physically well-motivated laboratory to explore collisional black hole formation and to assess how internal cluster properties regulate the efficiency of this process.

1.3 Observations of supermassive black holes

Observational evidence of black holes across cosmic time provides essential constraints on their formation and growth mechanisms. In the local Universe, the presence of supermassive black holes at the centers of galaxies is well established, offering insight into their present-day masses and host environments. Observations at progressively higher redshift probe the early assembly of these objects, constraining both their initial seed masses and the timescales available for growth.

1.3.1 Local Universe

In the local Universe, SMBHs are routinely detected at the centers of massive galaxies, where the gravitational potential is deepest (Volonteri, 2010; Barack et al., 2019). The most compelling dynamical evidence is provided by the Milky Way, where stellar-orbit measurements around Sagittarius A* reveal a central dark object of $\sim 4 \times 10^6\, M_\odot$ (Schödel et al., 2002; Ghez et al., 2008; Genzel et al., 2010). Similar measurements in nearby galaxies, such as M87, confirm the existence of SMBHs with masses up to $\sim 10^9\, M_\odot$ (Event Horizon Telescope Collaboration et al., 2019, 2022). These results demonstrate that fully assembled SMBHs are ubiquitous in the nuclei of present-day galaxies.

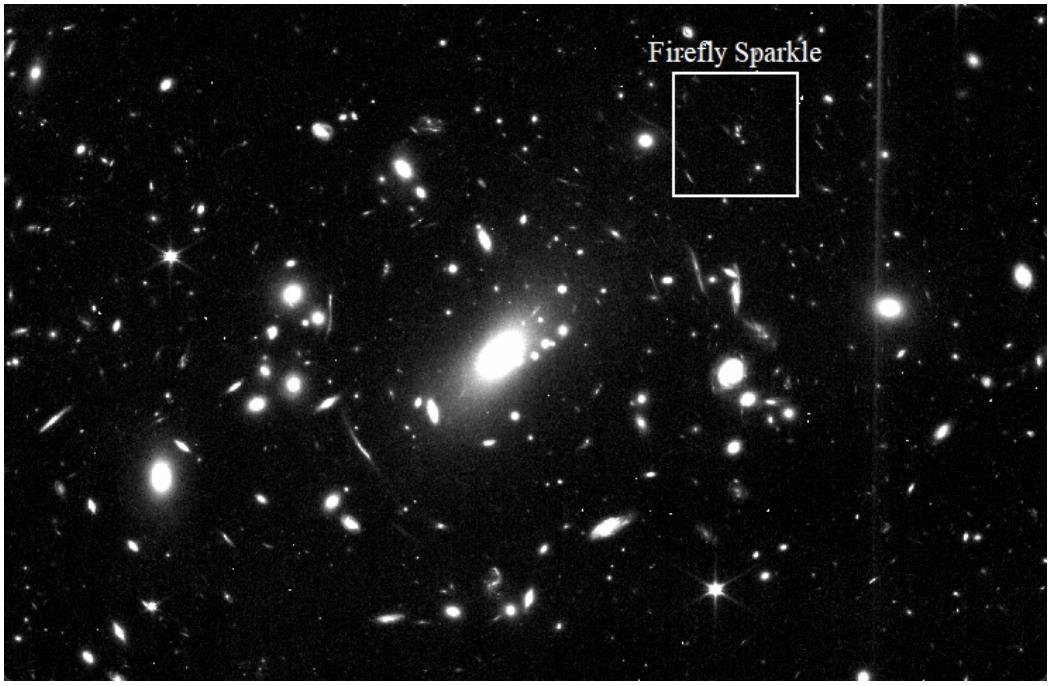

Figure 1.3.1: JWST NIRCam composite image of the field surrounding the galaxy cluster MACSJ1423.8+2404. The highlighted region marks the location of the system known as the *Firefly Sparkle*, identified and analyzed by Mowla et al. (2024) as one of the earliest observed stages in the assembly of a Milky Way–type galaxy, seen when the Universe was approximately 600 Myr old ($z \approx 8.3$). The image was produced from publicly available JWST observations retrieved from the Mikulski Archive for Space Telescopes (MAST). The annotation indicating the Firefly Sparkle region was added by the author for illustrative purposes. JWST data: © NASA, ESA, CSA, and STScI.

1.3.2 High redshift

One of the strongest constraints on SMBH formation arises from the limited cosmic time available for their early growth. Over the past four decades, advances in observational capabilities have steadily pushed the redshift frontier of quasar detections to earlier epochs. Initial discoveries of luminous quasars at $z \sim 4$ (Hazard and McMahon, 1985; Mitchell et al., 1990; Turner, 1991) already indicated that billion-solar-mass black holes existed when the Universe was only $\sim$ 1.2 Gyr old. Subsequent wide-field surveys, such as the Sloan Digital Sky Survey (SDSS) and other large optical programs, extended this limit to $z \sim 6$ (Fan et al., 2001; Barth et al., 2003; Willott et al., 2005; Jiang et al., 2016; Inayoshi et al., 2020), while more recent near-infrared campaigns have identified quasars at redshifts approaching $z \sim 10$–11 (Harikane et al., 2023; Natarajan et al., 2024; Maiolino

et al., 2024b,a; Mowla et al., 2024; Tripodi et al., 2025; Herrera-Camus et al., 2025).

Beyond luminous quasars, JWST observations have also revealed intensely star-forming galaxies at comparable epochs. One notable example is the *Firefly Sparkle* system at $z \approx 8.3$ (Figure 1.3.1), which hosts multiple compact stellar clusters with very high surface mass densities (Mowla et al., 2024). As discussed in Section 1.1, such environments are of particular interest as potential sites for the early assembly of massive black hole seeds, highlighting the growing observational evidence for dense stellar systems at high redshift.

The detection of supermassive black holes with inferred masses of $\gtrsim 10^8$–$10^9\,M_\odot$ at these redshifts implies that their formation and growth must have occurred within less than ~ 0.5 Gyr after the Big Bang. This timescale is significantly shorter than that inferred from the earliest quasar detections at $z \sim 4$, placing increasingly stringent constraints on models of early black hole growth.

This progressive tightening of the available growth time is illustrated in Figure 1.3.2, which compiles the population of known quasars at $z \gtrsim 6$ from optical and infrared surveys. The reference growth tracks shown in the figure correspond to black holes accreting continuously at the Eddington rate, with a radiative efficiency $\epsilon_{\mathrm{Edd}=0.1}$ starting from stellar-mass seeds with $M_\bullet = 10 M_\odot$ and $M_\bullet = 100 M_\odot$ for the lower and upper curve respectively, constraining the mass growth of SMBH at redshift $z \gtrsim 9$ to the order $\sim 10^8 M_\odot$ under the described conditions.

The presence of such massive black holes in the early Universe therefore constitutes one of the most severe empirical challenges for black hole formation models, strongly motivating scenarios that invoke either rapid early accretion phases or the formation of massive black hole seeds. Thus providing key observational impetus for exploring alternative seed-formation channels, including those operating in dense stellar environments.

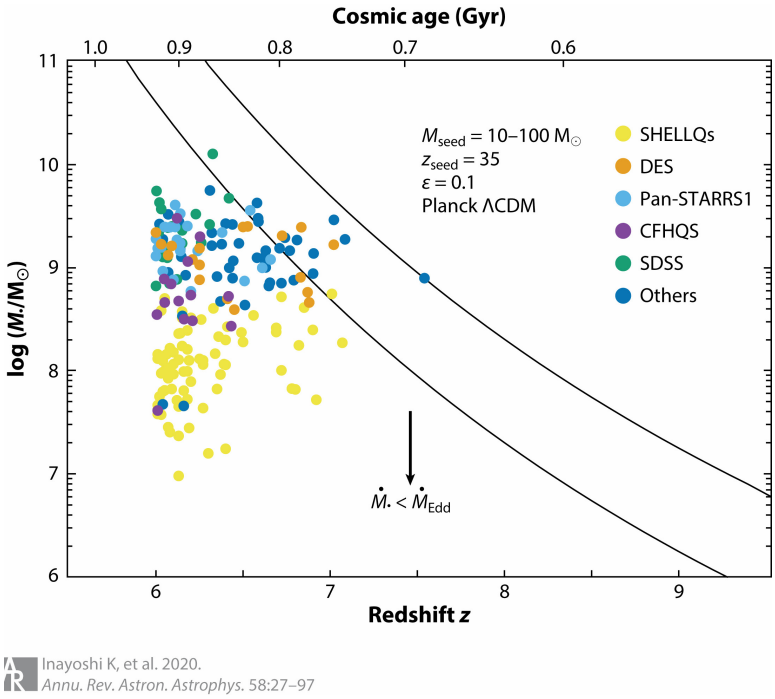

Figure 1.3.2: Distribution of known quasars at $z \gtrsim 6$, compiled from multiple optical and infrared surveys. Each point corresponds to an observed quasar whose black hole mass was inferred from rest-frame UV luminosities under the assumption of Eddington-limited accretion. The black curves indicate reference growth tracks for black holes accreting continuously at the Eddington rate from stellar-mass seeds. The large population of luminous quasars between $z \sim 6$ and $z \sim 8$ demonstrates that supermassive black holes with $M_\bullet \sim 10^{8\text{–}9}\, M_\odot$ were already in place less than a billion years after the Big Bang. Reproduced from Inayoshi, K., Visbal, E., & Haiman, Z. (2020), *Annual Review of Astronomy and Astrophysics*, 58, 27–97,

Chapter 2

Theoretical Framework

2.1 Theoretical Framework

This chapter presents the theoretical framework describing the dynamical evolution of dense stellar clusters and the physical mechanisms governing their internal interactions. It focuses on the collective and collisional processes that drive structural evolution in these systems, such as two-body relaxation, energy exchange, and stellar collisions, which together regulate the long-term stability and mass growth of cluster members.

The theoretical background discussed here provides the foundation for understanding how these processes can lead to runaway stellar mergers and the subsequent formation of massive black holes within cluster environments. Characteristic timescales and equilibrium models are introduced to offer analytical insight and to contextualize the numerical simulations presented in the following chapters.

2.2 Dynamical evolution of star clusters

2.2.1 Virial equilibrium

The virial theorem provides the fundamental baseline for describing the global dynamical state of stellar clusters. For an isolated self-gravitating system in dynamical equilibrium, the time-averaged kinetic energy T and gravitational

potential energy V satisfy

$$2T + V = 0, \tag{2.2.1}$$

where T denotes the total kinetic energy of the system and V its gravitational potential energy (Spitzer, 1987).

In numerical N-body simulations, star clusters are typically initialized close to virial equilibrium (Kroupa, 2008) in order to suppress strong initial transients and to ensure that the subsequent evolution is driven primarily by internal dynamical processes.

A useful diagnostic for quantifying departures from virial equilibrium is the *virial ratio*,

$$Q = \left| \frac{T}{V} \right|, \tag{2.2.2}$$

which measures the relative contribution of kinetic to potential energy in the system. Perfect virial equilibrium corresponds to $Q = 0.5$. During the dynamical evolution, deviations from this value reflect global structural changes: $Q > 0.5$ indicates that the kinetic energy temporarily exceeds the binding potential, leading to cluster expansion, whereas $Q < 0.5$ corresponds to a dynamically contracting configuration driven by sub-virial stellar velocities (Binney and Tremaine, 2008).

Satisfaction of the virial condition implies that the system is dynamically stable on crossing timescales, but does not necessarily indicate thermal or long-term equilibrium, i.e., even virialized systems may gradually depart from equilibrium over longer timescales as a result of two-body relaxation, mass loss, and collisional interactions, leading to structural evolution and changes in their internal density profiles.

2.2.2 Two-body relaxation and energy exchange

Stellar clusters are discrete systems composed of a finite number of stars, and their long-term evolution is governed by gravitational interactions between individual objects. Although close encounters are relatively rare, each star experiences a large number of weak, distant interactions with neighboring stars. The cumulative effect of these small-angle deflections leads to gradual changes in stellar velocities and trajectories, a process known as two-body relaxation.

Individual encounters conserve energy and momentum, but collectively they drive

a diffusive redistribution of kinetic energy in velocity space (Binney and Tremaine, 2008). Over time, this process transports energy from the dense central regions toward the outskirts of the cluster. As a result, while the system remains close to virial equilibrium on dynamical timescales, two-body relaxation governs its secular evolution on much longer timescales.

The efficiency of two-body relaxation is closely linked to the characteristic timescales of the system. A fundamental scale is the dynamical or crossing time, defined as the typical time required for a star to traverse the cluster,

$$t_{\rm cr} \sim \frac{R}{\sigma}, \tag{2.2.3}$$

where R is a characteristic cluster size and σ is the one-dimensional velocity dispersion. For a virialized system, this velocity scale is set by the cluster mass and size through the virial theorem,

$$\sigma \sim \sqrt{\frac{GM}{R}}. \tag{2.2.4}$$

Two-body relaxation operates on a timescale much longer than the crossing time. The relaxation time, $t_{\rm rel}$, represents the timescale over which cumulative encounters significantly alter a star's velocity by an amount comparable to its initial value. A commonly used order-of-magnitude estimate is

$$t_{\rm rel} \simeq \frac{0.1\,N}{\ln N}\, t_{\rm cr}, \tag{2.2.5}$$

where N is the total number of stars in the cluster. This process plays a central role in driving the long-term structural evolution of dense stellar systems.

2.2.3 Core collapse and mass segregation

A direct consequence of two-body relaxation is the gradual evolution of the internal structure of the cluster. Through repeated energy exchanges, more massive stars tend to lose kinetic energy and migrate toward the central regions, while lower-mass stars gain energy and move outward. This process, known as mass segregation, increases the central concentration of massive objects and steepens the density profile of the cluster core.

As kinetic energy is transported outward, the core progressively loses energy and contracts due to the negative heat capacity of self-gravitating systems. This contraction results in a rise in both central density and velocity dispersion, driving the system toward a phase of core collapse (Spitzer, 1987; Lynden-Bell and Eggleton, 1980; Makino, 1996). While this evolution is mediated by relaxation processes, its outcome is the formation of a dense central region in which close stellar encounters become increasingly frequent.

As such, it is useful to introduce a *local* relaxation time, which describes the efficiency of relaxation processes as a function of position within the cluster (Spitzer, 1987; Quinlan, 1996). Rather than characterizing the system globally, the local relaxation time captures how variations in stellar density and velocity dispersion lead to different evolutionary rates between the core and the outer regions. It can be written as

$$t_{\rm r} = \frac{0.065\, v_{\rm r}^3}{G^2\, m\, \rho_{\rm r}\, \ln(\Lambda)}, \tag{2.2.6}$$

where m is the mean stellar mass, $\rho_{\rm r}$ and $v_{\rm r}$ are the local stellar mass density and velocity dispersion, respectively, and $\ln(\Lambda)$ is the Coulomb logarithm.

When relaxation is evaluated within a radius enclosing half of the total cluster mass, $r_{\rm hm}$, the Coulomb logarithm can be estimated using the virial relation (Eq. (2.2.1)), yielding $\ln(\Lambda) \simeq \ln(0.4N)$ for an isolated system of N stars (Spitzer, 1987). Approximating the local quantities in Eq. (2.2.6) by their half-mass averages, $\rho_{\rm r} \to \rho_{\rm hm}$ and $v_{\rm r} \to \sigma$, leads to the definition of the initial half-mass relaxation time

$$t_{\rm rh} = \frac{0.138\, N}{\ln(0.4N)} \left(\frac{r_{\rm hm}^3}{GM} \right)^{1/2}, \tag{2.2.7}$$

where M is the total cluster mass. This timescale is proportional to the global relaxation time introduced in Eq. (2.2.5) by a factor of order $(r_{\rm hm}/R)^{3/2}$.

A still shorter and more central relaxation timescale can be defined for the cluster core by evaluating Eq. (2.2.6) at the central density and velocity dispersion. Replacing $\rho_{\rm r}$ and $v_{\rm r}$ by their central values, ρ_0 and σ_0, one obtains the central relaxation time

$$t_{\rm rc} = \frac{0.065\, \sigma_0^3}{G^2\, m\, \rho_0\, \ln(0.4N)}, \tag{2.2.8}$$

which provides a natural measure of the dynamical timescale governing the

evolution of the cluster core.

Consequently in sufficiently dense environments, the combination of mass segregation and core contraction substantially enhances the probability of physical collisions between stars, therefore in this regime physical collisions between stars can no longer be neglected.

2.3 Stellar encounters in dense clusters

2.3.1 Close encounters and physical collisions

In dense stellar systems, the high stellar number density leads to frequent gravitational interactions between stars. Most of these interactions take the form of close encounters, during which stars undergo deflections in their trajectories due to mutual gravitational forces, without coming into direct physical contact. While individual encounters conserve energy and momentum, their cumulative effect plays a central role in driving the dynamical evolution of the cluster.

A subset of close encounters results in physical collisions when the minimum separation between two stars becomes smaller than the sum of their stellar radii, i.e.,

$$D < R_1 + R_2.$$

In such events, the stars may merge, producing a more massive stellar object. In dense cluster environments, where collision rates are enhanced by high central densities and gravitational focusing, repeated collisions involving the same star may occur.

If a single object undergoes multiple successive mergers, it can experience runaway mass growth, eventually forming a very massive star. Such objects are potential progenitors of intermediate-mass black holes, provided they avoid premature disruption due to stellar evolution or mass loss (Portegies Zwart et al., 1999; Portegies Zwart and McMillan, 2002; Glebbeek et al., 2009; Volonteri, 2010; Glebbeek et al., 2013; Escala, 2021; Vergara et al., 2022). This collisional growth channel is therefore of particular relevance in dense stellar systems and constitutes the primary black hole formation pathway explored in this work.

2.3.2 Gravitational focusing and collisional cross section

In dense stellar environments, close encounters between stars do not follow purely ballistic trajectories. Instead, mutual gravitational attraction can significantly bend their orbits, increasing the probability of close approaches and physical collisions. This effect, known as *gravitational focusing*, enhances the effective collisional cross section beyond its purely geometric value and plays a central role in determining collision rates in star clusters.

The strength of gravitational focusing is commonly characterized by the Safronov number (Binney and Tremaine, 2008), defined as the ratio between the stellar surface escape velocity and the velocity dispersion of the cluster,

$$\Theta = \frac{v_{\rm esc}^2}{4\sigma^2}, \tag{2.3.1}$$

where $v_{\rm esc}$ is the escape velocity from the stellar surface and σ is the one-dimensional velocity dispersion of the system. For stellar encounters, this quantity can be expressed as

$$\Theta = 9.54\,\frac{m_\star R_\odot}{M_\odot R_\star}\left(\frac{100\ \mathrm{km\ s^{-1}}}{\sigma}\right)^2, \tag{2.3.2}$$

explicitly highlighting its dependence on stellar compactness and cluster kinematics.

Including gravitational focusing, the effective collisional cross section for two stars can be written as

$$\Sigma_0 = 16\sqrt{\pi}\,R_\star^2\,(1+\Theta)\,, \tag{2.3.3}$$

where the first term corresponds to the geometric cross section and the second accounts for the enhancement due to gravitational focusing. In the regime $\Theta \gg 1$, which is typical of dense clusters with low velocity dispersion, gravitational focusing dominates and substantially increases the likelihood of stellar collisions.

The enhancement of the collisional cross section due to gravitational focusing directly impacts the rate at which stellar collisions occur. To quantify the importance of collisional processes in dense clusters, it is therefore necessary to introduce a characteristic timescale for stellar collisions and to compare it with other relevant dynamical and evolutionary timescales.

2.3.3 Collisional timescale and collision rates

In sufficiently dense stellar environments, physical collisions between stars may occur on timescales comparable to, or shorter than, the evolutionary timescales of massive stars. The characteristic timescale for stellar collisions can be expressed as

$$t_{\rm coll} \sim \frac{1}{n\,\Sigma\,\sigma}, \tag{2.3.4}$$

where n is the local stellar number density, Σ is the effective collisional cross section, and σ is the velocity dispersion of the system (Binney and Tremaine, 2008). As discussed in the previous section, gravitational focusing can significantly enhance the cross section in low-velocity, high-density environments, making collisions particularly efficient in cluster cores.

The strong dependence of $t_{\rm coll}$ on density implies that collisional processes are highly localized, with the highest collision rates occurring in the central regions of dense clusters. As a result, the collisional evolution of a cluster is often dominated by its core, especially during phases of contraction or core collapse.

However, for the purpose of comparing different systems and guiding numerical experiments, it is useful to make use of a global condition, expressed in terms of characteristic cluster parameters. This motivates the introduction of critical density and mass associated with the onset of collision-dominated evolution.

2.3.4 Critical mass

Analytical arguments indicate that stellar collisions become dynamically important when the characteristic collision timescale, $t_{\rm coll}$, is comparable to or shorter than the evolutionary timescale of the system, t_H (Escala, 2021). In this regime, collisional processes may dominate the dynamical evolution of the cluster and potentially lead to runaway growth.

Under reasonable assumptions for the stellar mass function and dimensionless factors of order unity, this condition can be expressed as a critical density threshold,

$$\rho_{\rm crit} \equiv \left(\frac{4\pi m_\star}{300\,R_\star^2\,t_H\,G^{1/2}}\right)^{2/3} \leq M R^{-7/3}, \tag{2.3.5}$$

where $m_\star$ and $R_\star$ are the characteristic stellar mass and radius, respectively, and

t_H represents the characteristic evolutionary timescale of the system. The quantity $\rho_{\rm crit}$ has dimensions intermediate between a volumetric density ($\propto R^{-3}$) and a surface density ($\propto R^{-2}$).

For reference, a system composed of solar-mass stars with solar radii evolving over a timescale of $t_H \sim 10^{10}\,\mathrm{yr}$ yields a minimum critical density of $\rho_{\rm crit} \sim 10^7\,M_\odot\,\mathrm{pc}^{-7/3}$.

From the critical density, a corresponding critical mass can be defined (Vergara et al., 2022) by assuming a characteristic cluster size R,

$$M_{\rm crit} = \left(\frac{4\pi m_\star}{300\,R_\star^2\,t_H\,G^{1/2}}\right)^{2/3} R^{7/3}. \tag{2.3.6}$$

In the context of this work, the timescale t_H is identified with the total simulation time.

Figure 2.3.1 illustrates how the resulting critical mass depends on the initial cluster properties for different characteristic stellar masses and numbers of stars, evaluated at a fixed evolutionary time of $t_H = 10$ Myr. Models with identical numbers of stars N and mean masses $m_\star$ are indicated by the same symbols, while the shaded regions capture variations arising from different initial velocity dispersions.

The figure therefore delineates the region of parameter space in which stellar collisions are expected to become dynamically significant within the adopted timescale, providing a physically motivated threshold for the onset of collisional runaway. In this sense, $M_{\rm crit}$ serves as a benchmark against which different cluster models can be compared, independent of their absolute mass or size.

The critical mass provides a useful reference scale for identifying clusters in which collisional processes are expected to become dynamically relevant. In practice, this quantity is most informative when employed in conjunction with outcome-based diagnostics that characterize the efficiency of compact object formation. In particular, comparing the initial cluster mass normalized by its critical value to the resulting black hole formation efficiency allows systematic trends between global cluster properties and runaway outcomes to be identified. This motivates the introduction of the black hole formation efficiency as a complementary measure, which will be explored and quantified using numerical simulations in the following sections.

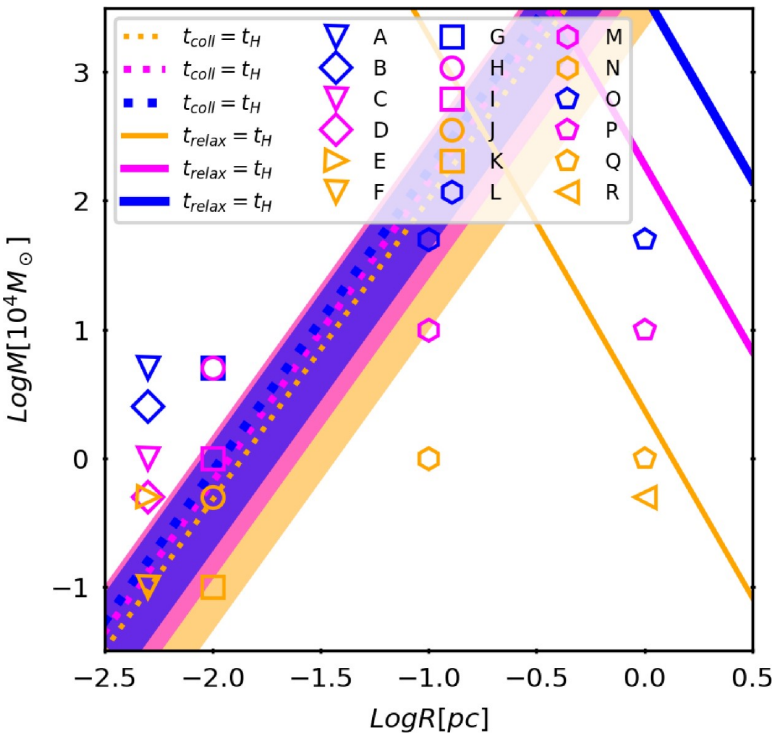

Figure 2.3.1: Critical mass condition for the onset of dynamically significant stellar collisions in dense star clusters. Blue, magenta, and orange symbols, curves, and shaded regions correspond to characteristic stellar masses of $m_\star = 50$, 10, and 1 $M_\odot$, respectively, with identical symbols indicating models with the same number of stars N. The curves illustrate the dependence of the critical cluster mass on global cluster properties at a fixed evolutionary time of $t_H = 10$ Myr, while the shaded regions reflect variations associated with different initial velocity dispersions. This figure serves as a reference scale for identifying regions of parameter space in which collisional processes are expected to become dynamically dominant and potentially lead to runaway growth. Reproduced from Vergara et al. (2022), Figure 1, *Monthly Notices of the Royal Astronomical Society*, 522, 4224–4237, © 2023 The Author(s).

2.3.5 Expected black hole formation efficiency

A convenient way to quantify the outcome of collisional runaway is through the black hole formation efficiency, defined as the fraction of the initial cluster mass that is ultimately converted into a black hole remnant. In the absence of gas accretion and external mass inflow, this efficiency can be expressed as

$$\epsilon_{\rm BH} = \frac{M_{\rm BH}}{M_{\rm ini}}, \tag{2.3.7}$$

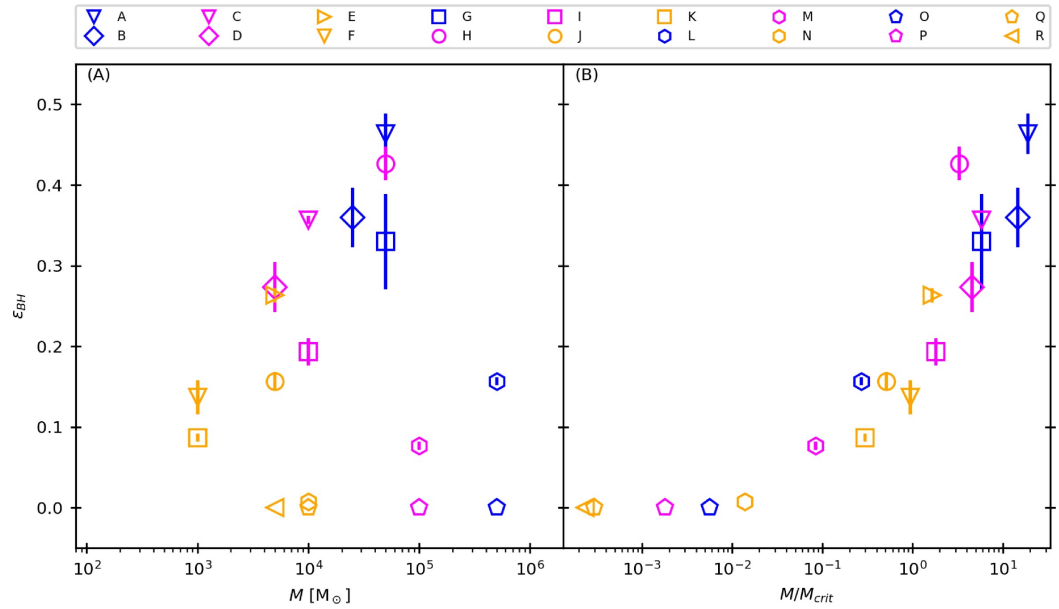

Figure 2.3.2: Black hole formation efficiency evaluated at $t_H = 10$ Myr as a function of the initial nuclear star cluster mass. Left panel (A): black hole formation efficiency, originally introduced as $\epsilon_{\rm BH} = (1 + M_{\rm NSC}/M_{\rm BH})^{-1}$ and mathematically equivalent to Equation (2.3.7), plotted against the initial cluster mass M. Right panel (B): the same efficiency plotted as a function of the initial cluster mass normalized by the critical mass $M_{\rm crit}$. Normalizing by $M_{\rm crit}$ reveals a tighter correlation across different cluster models, indicating that the critical mass provides a relevant physical scale for black hole formation via collisional runaway. Reproduced from Vergara et al. (2022), Figure 5, *Monthly Notices of the Royal Astronomical Society*, 522, 4224–4237, © 2023 The Author(s).

where $M_{\rm ini}$ is the total initial mass of the stellar cluster and $M_{\rm BH}$ is the mass of the resulting black hole seed.

The black hole formation efficiency $\epsilon_{\rm BH}$ depends sensitively on the collisional timescale, the duration of the runaway phase, and the interplay between stellar dynamics and stellar evolution. As a result, clusters with broadly similar global properties may nevertheless exhibit markedly different efficiencies. A useful way to characterize this behavior is to express the efficiency as a function of both the initial cluster mass and its ratio to the critical collisional threshold introduced above.

Figure 2.3.2 illustrates the black hole formation efficiency evaluated at $t_H = 10$ Myr as a function of the initial cluster mass M (panel A) and of the mass normalized by the corresponding critical value $M/M_{\rm crit}$ (panel B). When plotted against the absolute cluster mass, the efficiency displays substantial scatter across different

models. In contrast, normalizing by $M_{\rm crit}$ reveals a significantly tighter and more systematic trend, indicating that the critical mass captures the relevant combination of cluster properties that governs the onset and outcome of collisional runaway.

This normalization therefore provides a physically motivated framework for comparing clusters with different initial conditions on equal footing.

2.4 Equilibrium models of star clusters

In order to initialize dynamically relaxed star clusters for direct N-body simulations, it is customary to adopt equilibrium distribution functions that approximate the quasi-stationary states established through two-body relaxation. Static equilibrium models provide self-consistent, time-independent representations of stellar systems that minimize artificial transients and spurious initial collisions, ensuring that the subsequent evolution is driven primarily by internal dynamical processes such as relaxation, mass segregation, and stellar collisions.

The foundation of these equilibrium models lies in the use of the stellar *specific energy*, expressed as a function of position and velocity,

$$E(r, v) = \frac{1}{2}v^2 - V(r), \tag{2.4.1}$$

where $V(r)$ denotes the gravitational potential per unit mass. For a system in equilibrium, the potential must satisfy the Poisson equation,

$$\nabla^2 V = 4\pi G\rho(r), \tag{2.4.2}$$

with $\rho(r)$ the local mass density. The latter is obtained by integrating the phase-space distribution function $f(E)$ over all velocities,

$$\rho(r) = 4\pi \int_0^\infty f(E)\, v^2\, dv, \tag{2.4.3}$$

where $f(E)$ implicitly represents the mass density in phase space, such that the total mass is recovered by integrating f over all positions and velocities.

In this formulation, the distribution function depends only on the specific energy in the case of isotropic, non-rotating systems. More complex models may include

additional integrals of motion, such as the z-component of the angular momentum J_z, leading to distribution functions of the form $f(E, J_z)$, a formalism used to describe rotating equilibrium configurations, such as the *rotating King model* introduced later in Section 2.4.4.

Several classical equilibrium models have been developed to represent self-gravitating stellar systems of increasing physical realism. The simplest of these is the Plummer (1911) model, which assumes an isotropic velocity distribution and yields an analytic, finite-mass configuration with a smooth central core. The *isothermal sphere*, by contrast, represents a more physically motivated model in which the stellar velocities follow a Maxwellian distribution with constant velocity dispersion, approximating the end state of a relaxed, collisional system (Spitzer, 1987).

A further refinement is provided by the King (1966) family of models, which incorporate an energy truncation to mimic the effect of a tidal boundary and introduce a dimensionless concentration parameter that controls the ratio between the cluster's core and tidal radii. These models reproduce the surface brightness profiles of observed globular clusters with remarkable fidelity and have therefore become the standard choice for initializing realistic N-body simulations.

The following subsections summarize these equilibrium configurations,beginning with the analytic Plummer model, followed by the isothermal sphere and the non-rotating King model. Finally, extensions of the King formalism based on Fokker–Planck treatments, including rotating equilibrium configurations (Lagoute and Longaretti, 1996; Longaretti and Lagoute, 1996, 1997; Einsel and Spurzem, 1999), are introduced, as they provide the theoretical foundation for the rotating cluster models employed in the simulations presented in this work.

2.4.1 The Plummer (1911) model

A historically important and analytically tractable equilibrium configuration is the Plummer (1911) model, which provides a finite-mass, spherically symmetric, and isotropic stellar system that approximates the central structure of relaxed clusters. The model belongs to the family of so-called *polytropic spheres*, characterized by a power-law dependence of the distribution function on the specific energy. In

general form, the distribution function can be written as

$$f(E) = \begin{cases} k\,(-E)^p, & E < 0, \\ 0, & E \geq 0, \end{cases} \tag{2.4.4}$$

where E is the specific energy, k is a normalization constant, and p is an index related to the polytropic exponent $n = p + 3/2$. The Plummer model corresponds to the particular case $n = 5$, which yields a simple analytic solution with finite total mass and potential.

The associated mass density profile is

$$\rho(r) = \frac{3M}{4\pi a^3}\left(1 + \frac{r^2}{a^2}\right)^{-5/2}, \tag{2.4.5}$$

where M is the total mass and a is a characteristic scale radius related to the half-mass radius by $r_{\rm hm} \simeq 1.305\,a$ (Kroupa, 2008). The corresponding gravitational potential is

$$V(r) = -\frac{GM}{\sqrt{r^2 + a^2}}. \tag{2.4.6}$$

The Plummer model is finite everywhere, possessing a smooth central core and an outer density fall-off $\rho \propto r^{-5}$ that guarantees a finite total mass. Owing to its analytic simplicity, isotropy, and absence of adjustable concentration parameters, it remains a standard reference for code validation and pedagogical demonstrations of self-gravitating systems in equilibrium. However, its relatively shallow outer density profile makes it less suitable for modeling tidally truncated clusters. For this reason, more realistic equilibrium distributions, such as the King (1966) models, are often preferred when reproducing the structure of observed globular clusters or initializing direct N-body simulations.

2.4.2 Isothermal spheres

A more physically motivated equilibrium configuration for a self-gravitating stellar system is the *isothermal sphere* (Spitzer, 1987; Binney and Tremaine, 2008). It is obtained by assuming that the stellar velocities follow a Maxwellian distribution with a spatially uniform velocity dispersion σ. Under this assumption, the distribution function depends only on the stellar specific energy E and can be

written as

$$f^{(0)}(E) = k\, e^{-\beta E}, \tag{2.4.7}$$

where k is a normalization constant and $\beta^{-1} \propto \sigma^2$ represents a measure of the mean squared stellar velocity or "temperature" of the system.

The corresponding density distribution is determined by integrating the distribution function over all velocities, yielding

$$\rho(r) = \rho_0 \exp\left[-\frac{V(r)}{\sigma^2}\right], \tag{2.4.8}$$

where ρ_0 is the central density and $V(r)$ the corresponding gravitational potential. The formal solution describing an isothermal, self-gravitating sphere can also be obtained by directly solving the dimensionless form of Poisson's equation coupled to the Maxwellian distribution function. When this equation is integrated with the boundary conditions of finite central density and vanishing gradient at the center (i.e. $\rho(0) = \rho_0$ and $d\rho/dr|_{r=0} = 0$), the resulting profile is well behaved at small radii and approaches $\rho(r) \propto r^{-2}$ at large radii, thereby matching the expected behavior of the singular solution in the outer regime. This configuration is referred to in the literature as the *non-singular isothermal sphere*. Unlike the singular case, however, the full non-singular solution cannot be expressed in closed analytic form and must be obtained numerically by integrating the underlying structure equation (e.g. Binney and Tremaine, 2008). Because of this, a number of analytic approximations have been developed that reproduce the numerically determined density stratification to high accuracy across the entire radial domain, including recently proposed prescriptions that match both the inner core behavior and the asymptotic r^{-2} fall-off with small relative error (e.g. Raga et al., 2013; Natarajan and Lynden-Bell, 1997). These non-singular solutions provide a more realistic theoretical reference than the singular isothermal sphere, yet they remain idealized and do not represent finite-mass systems without additional truncation.

Despite its lack of a finite total mass and outer boundary, the isothermal sphere provides valuable theoretical insight into the structure of relaxed stellar systems. Its constant velocity dispersion captures the essential outcome of long-term collisional relaxation, in which kinetic energy is redistributed until a nearly isothermal state is achieved. In practice, however, real clusters are tidally limited and cannot reach such a global equilibrium.

Because of these shortcomings, the isothermal sphere serves primarily as a reference or limiting case for more realistic equilibrium distributions. The King (1966) models address these issues by introducing a high-energy truncation that imposes a finite tidal boundary. In the limit of increasing central concentration, the King models asymptotically approach the isothermal sphere, thereby providing a smooth physical connection between both descriptions.

2.4.3 The non-rotating King (1966) model

A physically motivated class of equilibrium models was introduced by King (1962, 1966), who demonstrated that many globular clusters share a common structural form characterized by a dense core and a finite outer extent. In his 1962 observational study, King proposed an empirical surface-density law that successfully reproduced the projected light profiles of Galactic globular clusters,

$$\Sigma(r) = k \left[\frac{1}{\sqrt{1 + (r/r_c)^2}} - \frac{1}{\sqrt{1 + (r_t/r_c)^2}} \right]^2 , \tag{2.4.9}$$

where $\Sigma(r)$ is the projected stellar surface density, r_c is the core radius, r_t the tidal (or truncation) radius, and k a normalization constant. This relation describes a nearly constant-density core followed by a steep decline near the cluster boundary, consistent with the finite spatial extent observed in globular clusters. The empirical success of this law motivated the theoretical development of the self-consistent King (1966) models, which reproduce the same structural behavior from first principles.

The *King models* can be interpreted as steady-state solutions of the Fokker–Planck equation for collisional stellar systems (Chandrasekhar, 1943; King, 1965). In this framework, the Fokker–Planck formalism describes how two-body relaxation shapes the stellar energy distribution toward equilibrium. King solved the time-independent form of this equation to obtain a self-consistent, truncated equilibrium model in which relaxation and stellar escape through the tidal boundary are balanced. The resulting equilibrium distribution therefore describes a dynamically relaxed, truncated system.

In this framework, relaxation tends to establish an approximately isothermal velocity distribution that is truncated at the escape energy. This truncation

accounts for stars with sufficient energy to leave the system, introducing a physically motivated boundary that limits the cluster's extent. The resulting phase-space distribution can be expressed as a *lowered Maxwellian*,

$$f(E) = \begin{cases} k\, e^{-2j^2 V_0} \left(e^{-2j^2 E} - 1 \right), & E < 0, \\ 0, & E \geq 0, \end{cases} \tag{2.4.10}$$

where E is the stellar specific energy, V_0 the central potential, j^2 a constant inversely proportional to the square of the central velocity dispersion, and k a normalization constant.

It is convenient to define the dimensionless potential

$$W \equiv -2j^2 V, \tag{2.4.11}$$

so that the model is fully specified by the central value $W_0 = -2j^2 V_0$. This dimensionless parameter provides a direct measure of the cluster's concentration: models with larger W_0 values exhibit denser cores and steeper outer profiles, approaching the isothermal sphere in the limit of very large W_0. Conversely, models with intermediate concentration ($2.5 \lesssim W_0 \lesssim 7.5$) yield profiles similar to the Plummer model (Kroupa, 2008; Spurzem and Kamlah, 2023), providing a useful point of comparison between both distributions.

An alternative but equivalent characterization of the model concentration is given by the concentration parameter

$$c \equiv \log \left(\frac{r_t}{r_k} \right), \tag{2.4.12}$$

where r_t is the tidal radius (the outer boundary of the system) and r_k the King core radius, defined as

$$r_k = \left(\frac{9\sigma^2}{4\pi G \rho_0} \right)^{1/2}, \tag{2.4.13}$$

with σ the central velocity dispersion and ρ_0 the central mass density. Both W_0 and c encode the same structural information and uniquely determine the equilibrium density and velocity profiles of the model.

Because the central density and velocity dispersion increase systematically with

W_0, King models provide a natural framework for studying how initial cluster concentration influences relaxation-driven processes such as mass segregation and core contraction. The strong dependence of the relaxation time on W_0 makes them particularly useful for connecting equilibrium structure with subsequent dynamical evolution. These properties motivate the use of King models as initial conditions for direct N-body simulations, as well as their extension to more general equilibrium configurations.

Despite their wide applicability, the original King models remain idealized. They are single-mass, isotropic, and non-rotating, and they do not explicitly account for binaries, mass segregation, or angular momentum. Furthermore, they cannot describe clusters undergoing deep core collapse or strong departures from equilibrium. These limitations have led to the development of more general equilibrium models based on Fokker–Planck formalisms, which include rotation while retaining a quasi-static configuration. Nevertheless, the non-rotating King models continue to provide a physically grounded and computationally robust baseline for studying the dynamical pathways to runaway collisions and black hole formation.

2.4.4 Rotating equilibrium models

Classical King models assume spherical symmetry and an isotropic velocity distribution, and therefore neglect the presence of global rotation. However, observational evidence indicates that many star clusters and galactic nuclei exhibit measurable internal rotation, which influences both their structural morphology and long-term dynamical evolution. To account for this, the King formalism can be generalized by introducing angular momentum as an additional isolating integral of motion. This leads to the so-called *rotating King models* developed in the series of studies by Lagoute and Longaretti (1996) and later extended by Einsel and Spurzem (1999). These models provide self-consistent equilibrium distributions for axisymmetric, rotating stellar systems.

The stellar distribution function of a rotating King model depends on both the specific energy E and the z-component of the specific angular momentum J_z, and

can be written as

$$f(E, J_z) = \begin{cases} k e^{-\beta \Omega_0 J_z} \left(e^{-\beta E} - 1 \right), & E < 0 \\ 0, & E \geq 0, \end{cases} \tag{2.4.14}$$

where β is inversely proportional to the central velocity dispersion, analog to j^2 in the non-rotational King model and therefore related to W_0, while Ω_0 sets the strength of the initial rotation. The exponential term $\exp(-\beta \Omega_0 J_z)$ introduces an azimuthal bias in the velocity distribution, producing a flattened, oblate configuration whose degree of flattening increases with Ω_0. The equilibrium potential and density are determined self-consistently by solving the Poisson equation, resulting in an axisymmetric model with the rotation axis conventionally aligned with the z-direction.

As in the non-rotating King model, the distribution is truncated at the escape energy ($E = 0$) to ensure a finite spatial extent, but the inclusion of J_z couples the energy and angular-momentum structure through centrifugal support. The dimensionless rotation strength is characterized by the parameter ω_0, defined as

$$\omega_0 \equiv \Omega_0 r_k \sigma^{-1} = 3\, \Omega_0 (4\pi G \rho_0)^{-1/2}, \tag{2.4.15}$$

where r_k is the king radius defined by Eq. (2.4.13), ρ_0 is the central density of the cluster and σ the dispersion velocity. Physically, ω_0 measures the ratio of rotational to gravitational binding energy. Equilibrium configurations exist only for a restricted range of (W_0, ω_0) pairs: for a given concentration W_0, the rotation parameter cannot exceed a critical value beyond which centrifugal forces unbind the system. Increasing ω_0 leads to greater flattening and lower central concentration, whereas high W_0 values permit only moderate rotation before the equilibrium becomes unstable.

The inclusion of rotation introduces qualitatively new dynamical behavior. Angular momentum transport through two-body relaxation drives a secular redistribution of rotation, spinning down the outer layers while spinning up the core. This coupling of energy and angular momentum evolution can lead to the so-called *gravo–gyro catastrophe* (Hachisu, 1979, 1982), an analogue of the gravothermal catastrophe in non-rotating systems, in which core contraction is accompanied by differential spin-up and enhanced mass loss.

Early numerical studies based on these models showed that rotation accelerates the dynamical evolution of clusters. Using the modified King framework, Lagoute and Longaretti (1996) found that rapidly rotating clusters eject stars more efficiently during the early evolutionary stages, depleting angular momentum through escaping stars and thereby reducing the rotation amplitude over time. Later, Einsel and Spurzem (1999) employed the two-dimensional, orbit-averaged Fokker–Planck equations in (E, J_z) space to construct dynamically consistent single-mass rotating equilibria, showing that strong initial rotation can initially accelerate core concentration but subsequently enhances mass loss and core heating. The method was later refined by Kim et al. (2002), who included binaries as internal heating sources relevant to gravo-gyro and gravothermal oscillations. Their work, and subsequent multi-mass extensions (Kim et al., 2004), demonstrated that rotating clusters evolve faster than non-rotating ones due to enhanced relaxation and preferential escape of stars on prograde orbits.

In practical applications, rotating equilibrium models are generated using the FOPAX code (Einsel and Spurzem, 1999; Kim et al., 2002), which numerically solves the two-dimensional Fokker–Planck equations for $f(E, J_z)$ to produce particle realizations characterized by a given (W_0, ω_0). The models are constructed in dimensionless units, divided into a set of concentric shells each with a specified degree of rotation. Providing dynamically relaxed, axisymmetric initial conditions that extend the classical King models by including internal angular momentum while retaining a quasi-static equilibrium suitable for direct N-body evolution.

2.5 Core collapse timescales in equilibrium clusters

The initial concentration of a King model has a direct impact on the subsequent dynamical evolution of the cluster. Previous studies have shown that systems with higher central concentration undergo core collapse on significantly shorter timescales than less concentrated configurations (Quinlan, 1996). Since core collapse is characterized by a rapid increase in central density, this dependence has important implications for the onset of close stellar encounters, collisional processes, and the conditions required for runaway stellar growth.

Table 2.5.1 summarizes the dependence of the core-collapse timescale on the initial concentration of isolated non-rotational King models, parameterized by

W_0	c	$t_{\rm rc}/t_{\rm rh}$	$t_{\rm cc}/t_{\rm rc}$	$t_{\rm cc}/t_{\rm rh}$
1.0	0.296	1.032123	18.	18.12
2.0	0.505	0.859156	21.	17.94
3.0	0.672	0.678293	26.	17.70
4.0	0.840	0.502196	34.	17.33
5.0	1.029	0.341928	48.	16.45
6.0	1.255	0.205136	71.	14.56
7.0	1.528	0.098544	110.	10.90
8.0	1.833	0.032641	179.	5.84
9.0	2.118	0.007875	289.	2.28
10.0	2.350	0.002066	459.	0.95
11.0	2.548	0.000683	707.	0.48
12.0	2.739	0.000261	1018.	0.27

Table 2.5.1: Core-collapse timescales for isolated King models as a function of the central potential W_0. The ratios are reproduced from the numerical results of Quinlan (1996).

the dimensionless central potential W_0 (see Section 2.4.3). The table lists the corresponding the concentration parameter c (see Section 2.4.3, equation (2.4.12)), the ratio between the central and half-mass relaxation times $t_{\rm rc}/t_{\rm rh}$ (as defined in Section 2.2.3; equations (2.2.8) and (2.2.7)), and the core-collapse time $t_{\rm cc}$ expressed in units of both $t_{\rm rc}$ and $t_{\rm rh}$. All models considered by Quinlan (1996) share the same total number of stars and stellar mass spectrum and do not account for the influence of rotation, so differences in the collapse times arise solely from structural variations associated with W_0.

When measured in units of the half-mass relaxation time, $t_{\rm cc}/t_{\rm rh}$ decreases monotonically with increasing concentration. Highly concentrated clusters ($W_0 > 7$) are expected to experience core collapse on timescales that are more than an order of magnitude shorter than those of low-concentration systems. The half-mass relaxation time therefore provides a natural and physically meaningful reference scale for comparing the global dynamical evolution of clusters with different initial concentrations, since $t_{\rm rh}$ is defined by global properties of the system and is held fixed across the sequence of models with the same mass and number of stars.

By contrast, when the collapse time is expressed in units of the central relaxation time, $t_{\rm cc}/t_{\rm rc}$ increases strongly with W_0. This apparently opposite trend reflects the fact that the central relaxation time itself decreases rapidly as the concentration

increases, owing to the higher central densities and velocity dispersions in more concentrated King models. As a result, although core collapse occurs earlier in an absolute sense for high-W_0 systems, it corresponds to a larger number of local relaxation times measured at the cluster center. This highlights the importance of distinguishing between local and global relaxation processes when interpreting collapse timescales.

These results underscore the central role of two-body relaxation in the long-term evolution of globular clusters. Most Galactic globular clusters are well described by King models, indicating that they are close to relaxed, tidally truncated equilibria. Observational studies have shown that the majority of such clusters have intermediate concentrations, typically $W_0 \simeq 6$–8, while fewer than $\sim 10\%$ have low concentrations ($W_0 < 4$). A significant fraction, of order $\sim 20\%$, exhibit very high concentrations ($W_0 \gtrsim 10$) or cannot be adequately fitted by standard King models; these systems are commonly identified as core-collapsed or post-core-collapse clusters (Trager et al., 1995; Quinlan, 1996). Within this framework, the scaling relations derived by Quinlan (1996) provide a quantitative link between the observed distribution of cluster concentrations and their expected evolutionary behavior.

Chapter 3

Methodology

The formation and early growth of black holes in dense stellar systems is governed by strongly collisional dynamical processes, including two-body relaxation, mass segregation, coalescence and direct physical collisions between stars. Consequently, the study of collisional black hole formation requires numerical methods capable of resolving individual stellar encounters and close few-body interactions.

Several numerical approaches have been developed to model the evolution of star clusters, ranging from Fokker–Planck solvers and Monte Carlo methods to direct N-body simulations (Spurzem and Aarseth, 1996; Giersz, 1998; Einsel and Spurzem, 1999; Spurzem, 1999; Aarseth, 1999; Kroupa, 2008; Hypki and Giersz, 2013; Wang et al., 2016b; Leveque et al., 2022). While approximate techniques offer computational efficiency and are well suited for large-N systems in quasi-equilibrium, they rely on simplifying assumptions that limit their applicability in regimes dominated by strong encounters and runaway collisional processes. In particular, the treatment of stellar collisions and the formation of massive merger products often requires prescriptions that cannot fully capture the complexity of few-body dynamics.

In this work, we adopt a direct N-body approach, in which the equations of motion of all particles are integrated explicitly. This method provides the most accurate representation of collisional dynamics and allows for a self-consistent treatment of relaxation, close encounters, and physical collisions. Although computationally demanding, direct N-body simulations are essential for investigating the dependence of collisional black hole formation on cluster

concentration and rotation.

All simulations are performed using the NBODY6++GPU code, a highly optimized direct N-body integrator that combines high-order integration schemes with GPU acceleration (Nitadori and Aarseth, 2012; Wang et al., 2015, 2016b). The code includes treatments for stellar evolution, physical collisions, with high accuracy, i.e. typical energy error per crossing time $\Delta E/E < 10^{-5}$ (Spurzem and Kamlah, 2023), making it well suited for the study of dense and gravothermal systems over Myr timescales .

The scope of the present simulations is intentionally restricted in order to isolate the role of the main control parameters. All clusters are composed of equal-mass stars and do not include primordial binaries. While these simplifications limit the direct applicability of the results to real clusters, they allow for a controlled exploration of the physical mechanisms governing collisional black hole formation.

3.1 The NBODY6++GPU code

The NBODY6++GPU code integrates the equations of motion of all particles by directly evaluating their mutual gravitational interactions. For each particle i, the acceleration is obtained from the sum of pairwise Newtonian forces exerted by all other particles in the system. This fully explicit formulation allows the dynamical evolution of the cluster to be followed without resorting to approximation methods, which is essential for resolving relaxation-driven processes and strong few-body interactions in dense stellar systems.

Time integration is performed using a 4th-order Hermite integration scheme (Makino, 1991), which is based on a Taylor expansion of particle positions $\mathbf{r}_i$ and velocities $\mathbf{v}_i$ about the current time t_0. Using the values of position, velocity, acceleration $\mathbf{a}_{0,i}$, and its first time derivative (the jerk) $\dot{\mathbf{a}}_{0,i}$ evaluated at t_0, a predictor step is constructed as

$$\mathbf{r}_{p,i}(t) = \mathbf{r}_{0,i} + \mathbf{v}_{0,i}(t - t_0) + \mathbf{a}_{0,i}\frac{(t - t_0)^2}{2} + \dot{\mathbf{a}}_{0,i}\frac{(t - t_0)^3}{6}, \tag{3.1.1}$$

$$\mathbf{v}_{p,i}(t) = \mathbf{v}_{0,i} + \mathbf{a}_{0,i}(t - t_0) + \dot{\mathbf{a}}_{0,i}\frac{(t - t_0)^2}{2}, \tag{3.1.2}$$

where the subscript p denotes predicted quantities. At this stage, the predicted

positions and velocities provide only a low-order approximation and are used to re-evaluate the gravitational forces at the new time.

Based on the updated accelerations, the Hermite scheme applies a correction step that improves the solution without requiring explicit evaluation of derivatives higher than the first. Through Hermite interpolation, the corrected position and velocity are obtained as

$$\mathbf{r}_{1,i}(t) = \mathbf{r}_{p,i} + \mathbf{a}^{(2)}_{0,i}\frac{(t-t_0)^4}{24} + \mathbf{a}^{(3)}_{0,i}\frac{(t-t_0)^5}{120}, \tag{3.1.3}$$

$$\mathbf{v}_{1,i}(t) = \mathbf{v}_{p,i} + \mathbf{a}^{(2)}_{0,i}\frac{(t-t_0)^3}{6} + \mathbf{a}^{(3)}_{0,i}\frac{(t-t_0)^4}{24}, \tag{3.1.4}$$

where $\mathbf{a}^{(2)}_{0,i}$ and $\mathbf{a}^{(3)}_{0,i}$ denote the second and third time derivatives of the acceleration, constructed from differences between predicted and corrected forces.

The high accuracy of the Hermite scheme is complemented by adaptive time stepping, which allows the integrator to respond dynamically to the wide range of local dynamical conditions present within a star cluster. Particles experiencing strong accelerations or rapidly changing forces, such as those involved in close encounters or residing in the dense core, are naturally evolved with higher temporal resolution than particles in the outer regions.

To efficiently handle this range of timescales, NBODY6++GPU employs an individual time-step scheme, in which each particle is assigned its own time step based on local dynamical criteria (Aarseth, 1985).

$$\Delta t = \sqrt{\eta \frac{|\vec{a}| \cdot |\vec{a}^{(2)}| + |\vec{a}_0|^2}{|\vec{a}_0| \cdot |\vec{a}^{(3)}| + |\vec{a}^{(2)}|^2}} \tag{3.1.5}$$

With η as a free accuracy parameter, often set to be $\eta = 0.01 - 0.04$. These individual time steps are quantized into powers of two and grouped into blocks, so that particles with similar time steps can be advanced simultaneously. Hence the block time-step approach significantly reduces the computational cost relative to a global time-step scheme, while preserving the accuracy required to resolve fast dynamical processes.

To further reduce the computational cost of direct N-body integrations without sacrificing accuracy, NBODY6++GPU implements the Ahmad–Cohen neighbour

scheme (Ahmad and Cohen, 1973). This method exploits the fact that the gravitational force acting on a given particle can be naturally decomposed into two components: a rapidly varying contribution from nearby particles and a slowly varying contribution from distant ones, i.e., $\mathbf{a}_i = \mathbf{a}_{i,irr} + \mathbf{a}_{i,reg}$. Close neighbours dominate short-term force fluctuations and therefore require frequent updates, whereas distant particles contribute a smoother background force that evolves on longer timescales.

In practice, each particle is assigned a dynamically updated neighbour list within a specified radius. Forces from neighbour particles, $\mathbf{a}_{i,irr}$, are evaluated and updated at every short time step, while the contribution from distant particles, $\mathbf{a}_{i,reg}$, is computed less frequently and extrapolated using lower-order predictions. This separation significantly reduces the number of force evaluations per step, particularly in large-N systems, while preserving the accuracy required to resolve close encounters and relaxation-driven processes. The Ahmad–Cohen scheme is therefore essential for making long-term integrations of dense star clusters computationally feasible, especially when combined with individual and block time stepping.

While the Ahmad–Cohen neighbour scheme efficiently handles the frequent force updates required by nearby particles, it does not by itself resolve the numerical difficulties associated with extremely close encounters or tightly bound binaries. In such situations, the gravitational acceleration can become very large, forcing prohibitively small time steps and leading to a loss of numerical accuracy. To overcome this limitation, NBODY6++GPU employs Kustaanheimo–Stiefel (KS) regularization for close two-body interactions (Kustaanheimo et al., 1965; Aarseth, 2003). KS regularization is therefore crucial for modeling the dense central regions of star clusters, where close encounters are frequent and play a key role in driving collisional runaway and black hole formation.

The computational cost of direct N-body simulations scales as $\mathcal{O}(N)$ for particle force and $\mathcal{O}(N^2)$ for potential energy calculations, making parallelization essential for studying realistic star clusters. The NBODY family of codes has evolved progressively to address this challenge, starting from the original serial NBODY6 (Aarseth, 2003), through NBODY6++, which introduced distributed-memory parallelism via the Message Passing Interface (MPI) (Spurzem, 1999), and culminating in NBODY6++GPU, which incorporates hybrid CPU–GPU

acceleration (Nitadori and Aarseth, 2012; Wang et al., 2016b). In this framework, the most computationally demanding task, evaluation of gravitational forces, is offloaded to graphics processing units (GPUs), while CPUs handle integration control, neighbor schemes, and regularization procedures.

In addition to GPU acceleration, NBODY6++GPU employs a multi-level parallel strategy combining MPI for inter-node communication, shared-memory parallelism through OpenMP, and vectorization using SIMD instruction sets such as SSE and AVX. This hybrid approach allows the code to efficiently exploit modern high-performance computing architectures, achieving substantial speedups compared to earlier implementations. As a result, direct N-body simulations with up to $\sim 10^6$ particles have become feasible, enabling detailed studies of globular clusters and galactic nuclei with realistic particle numbers (e.g. Wang et al., 2015, 2016a; Shu et al., 2021). The integration of these parallelization techniques is therefore crucial for bridging the gap between theoretical N-body models and observed stellar systems.

Overall, NBODY6++GPU is especially well suited for the study of collisional stellar systems because it directly resolves gravitational interactions at the particle level while incorporating numerical techniques specifically designed to capture the multiscale nature of cluster dynamics. Adaptive time stepping and neighbor-based force evaluation ensure that both global evolution and localized strong encounters are treated consistently within the same simulation. Combined with efficient parallelization and GPU acceleration, these features enable simulations of dense star clusters at particle numbers approaching astrophysically relevant regimes, making NBODY6++GPU a robust and widely adopted tool for investigating the long-term dynamical evolution of collisional stellar systems.

Nevertheless, it is important to note that the treatment of stellar collisions and mergers in NBODY6++GPU is necessarily simplified when compared to hydrodynamical approaches. Collisions are handled through parametrized prescriptions, in which a fraction of the interacting stellar mass is transferred or lost according to results derived from detailed hydrodynamical studies in the literature, rather than being resolved self-consistently. In the simulations presented here, stellar evolution and collision outcomes are modeled using Package C as implemented in NBODY6++GPU **?**. While this approach allows collisions to be efficiently incorporated into large-N simulations, it introduces additional

uncertainties in the internal structure, mass retention, and subsequent evolution of merger products, which should be borne in mind when interpreting the results.

3.2 Stellar evolution, mass loss, and physical collisions

Previous studies have demonstrated that stellar mass loss plays a central role in shaping the dynamical evolution of dense star clusters and strongly influences the formation and growth of massive black hole seeds (Alister Seguel et al., 2020). In particular, mass loss affects the cluster's relaxation timescales, central density evolution, and the efficiency of collisional growth processes.

In NBODY6++GPU, mass loss arises primarily through two channels: stellar evolution and physical collisions. Stellar evolution is activated in the simulations by enabling the appropriate control parameters within the main input, which couple the dynamical integration to the internal stellar evolution routines. The role and configuration of these control parameters are described in detail in a later section devoted to the simulation input setup. Once stellar evolution is enabled, stars lose mass through stellar winds, evolutionary transitions between stellar phases, and compact-object formation (e.g. neutron stars and black holes). These processes are treated self-consistently alongside the gravitational dynamics and directly modify stellar masses and radii over time.

The stellar evolution prescriptions implemented in NBODY6++GPU are based on the widely used analytic models developed by Hurley et al. (2000, 2002, 2013a,b). Each particle is assigned a stellar type identifier corresponding to its evolutionary stage, with mass loss rates and radius evolution determined by its current state. For the purposes of this work, the most relevant stellar types include main-sequence (MS) stars, evolved helium-burning stars, and compact remnants such as black holes. While a detailed description of the full stellar evolution scheme is beyond the scope of this thesis, it is important to note that the evolution of stellar radii is explicitly tracked, as it directly affects the collision cross-sections and merger rates in dense environments.

Physical collisions are detected using a distance-based criterion following Kochanek (1992). A collision is assumed to occur when the pericenter distance between two

interacting bodies falls below an effective collision radius,

$$r_{\rm coll} = 1.7 \left(\frac{m_1 + m_2}{2m_1} \right) R_1, \tag{3.2.1}$$

where m_1 and R_1 correspond to the mass and radius of the primary star. When this condition is satisfied, the stellar evolution routines are invoked to construct a merger product with updated mass, radius, and evolutionary state. In collisions involving stars at different evolutionary stages, this process can result in partial rejuvenation of the merger product (Tout et al., 1997; Vergara et al., 2025).

The treatment of mass loss during collisions depends on the nature of the encounter and the types of objects involved. For most bound or low-velocity star–star mergers, particularly between MS stars, collisions are assumed to be largely conservative in mass, with the merger product retaining nearly the total mass of the progenitors. In contrast, high-velocity or hyperbolic star–star encounters are modeled using prescription-based mass-loss schemes, in which a fraction of the secondary star's mass is removed during the collision, typically of order a few tens of percent.

Collisions involving black holes are treated in a simplified, parameterized manner. When a star collides with a black hole, only a fraction of the stellar mass is accreted onto the compact object, while the remaining mass is assumed to be lost from the system. The accreted mass fraction can be adjusted through the input parameters of NBODY6++GPU; in this work, the default prescription is adopted, corresponding to approximately 50% of the stellar mass being lost during the collision. This approach does not attempt to model the detailed hydrodynamics of tidal disruption or accretion flows, but instead provides an effective subgrid description suitable for long-term dynamical simulations of dense stellar systems.

It is important to note that the stellar evolution prescriptions implemented in NBODY6++GPU are calibrated primarily for stars with masses up to $\sim 50\,M_\odot$. In the case of very massive merger products formed through runaway collisions, the combined effects of rejuvenation and the limitations of the stellar evolution model can delay the collapse of the object into a BH. As a consequence, the merger product remains classified as a stellar object for an extended period, retaining a radius that is orders of magnitude larger than that of a compact remnant. This substantially increases its geometric collision cross-section, making it more

susceptible to further collisions than it would be if it had already collapsed into a BH. As a result, the masses of the most massive objects formed through runaway growth may be overestimated prior to compact-object formation. This limitation should therefore be kept in mind when interpreting the final masses of IMBH candidates in the simulations.

3.3 Cluster models

The numerical simulations presented in this work are organized into three main sets of idealized star cluster models, hereafter referred to as the low-mass (LM), mid-mass (MM), and high-mass (HM) sets. In all cases, clusters are composed of equal-mass stars and are intentionally designed as controlled "toy" models, allowing us to systematically isolate the effects of two key parameters: the initial central concentration and the degree of rotation.

All clusters are evolved as isolated systems, without any external tidal field or galactic potential. Consequently, the total energy and angular momentum of each system are conserved, except for changes produced internally by stellar evolution and collisional mass loss. Each model is initialized in virial equilibrium, with a virial ratio of $Q = T/|V| = 0.5$, ensuring that the initial distribution function corresponds to a self-consistent equilibrium configuration for the adopted values of the dimensionless King concentration parameter W_0 and rotation parameter ω_0.

The low-mass set adopts a stellar mass of $m_\star = 0.58\,M_\odot$, corresponding to the mean stellar mass of a present-day stellar population according to widely used initial mass functions (IMFs; Salpeter 1955; Kroupa et al. 1993; Chabrier 2003; Bastian et al. 2010; Kroupa et al. 2024). These models serve as baseline representations of dynamically young, low-mass clusters in the local Universe, where stellar evolution and mass loss are expected to play a relatively minor role during the early dynamical evolution. Consequently, this set is anticipated to form the least massive black-hole (BH) candidates within the explored parameter space.

The mid-mass and high-mass sets adopt stellar masses of $m_\star = 10\,M_\odot$ and $m_\star = 50\,M_\odot$, respectively, representing extreme, top-heavy stellar populations. These systems experience stronger mass segregation, more frequent collisions, and are therefore expected to yield more massive BH candidates. Stellar evolution

Non-rotational model sets $\omega_0 = 0.0$				
Mass, set	$m_\star$ [$M_\odot$]	N	W_0	$t_{\rm rh}$ [Myr]
LM1	0.58	10k	2, 4, 6, 7, 8, 10, 12	1.030
LM2	0.58	25k	2, 4, 6, 7, 8, 10, 12	1.466
LM3	0.58	50k	2, 4, 6, 7, 8, 10, 12	1.929
MM1	10	10k	2, 4, 6, 7, 8, 10, 12	0.248
MM2	10	25k	2, 4, 6, 7, 8, 10, 12	0.353
HM	50	10k	2, 4, 6, 7, 8, 10, 12	0.110

Table 3.3.1: Set of non-rotating cluster models employed to isolate the impact of the initial central concentration. The concentration parameter W_0 is explored over a wider range than in the rotating models in order to quantify the effect of concentration independently of rotational support (i.e., $\omega_0 = 0$).

plays a dominant role in their evolution, particularly in the high-mass case, where a pronounced transition occurs at $\sim 5\,$Myr as most stars collapse into stellar-mass black holes. The associated reduction in stellar radii and masses leads to a sharp decline in the collision rate beyond this epoch.

Each mass set includes models with varying initial degrees of rotation, parameterized by the dimensionless rotation parameter ω_0. Non-rotating clusters correspond to $\omega_0 = 0.0$, while rotating models adopt $\omega_0 = 0.6$, 1.2, and 1.8. The value $\omega_0 = 1.8$ represents an extreme and likely non-physical case, but it is included to highlight the dynamical impact of strong initial rotation.

The initial concentration of the clusters is characterized by the dimensionless King parameter W_0. For non-rotating models, concentrations spanning $W_0 = 2, 4, 6, 7, 8, 10$, and 12 are explored in order to isolate the effect of concentration alone. The corresponding set of non-rotating models is summarized in Table 3.3.1, according to the their respective mean stellar mass $m_\star$ set, number of particles N, concentration W_0, and half-mass relaxation times $t_{\rm rh}$.

For rotating systems, the range of admissible concentrations is progressively restricted, reflecting the reduced set of physically consistent equilibrium solutions. In particular, models with $\omega_0 = 0.6$ extend up to $W_0 = 10$, those with $\omega_0 = 1.2$ up to $W_0 = 8$, and models with $\omega_0 = 1.8$ are limited to $W_0 \leq 7$, as summarized in Table 3.3.2.

To ensure a consistent and unbiased comparison of rotational effects, analyses involving different values of ω_0 are restricted to the common subset of

ω_0	Allowed W_0 range
0.0	$\{2, 4, 6, 7, 8, 10, 12\}$
0.6	$\{2, 4, 6, 7, 8, 10\}$
1.2	$\{2, 4, 6, 7, 8\}$
1.8	$\{2, 4, 6, 7\}$

Table 3.3.2: Range of dimensionless King concentration parameters W_0 for which equilibrium rotating King models could be constructed as a function of the rotation parameter ω_0. The restriction reflects the reduced set of physically consistent equilibria at increasing rotation and is independent of stellar mass and particle number.

Rotational models subsets					
Mass set	$m_\star$ [$M_\odot$]	N	W_0	ω_0	$t_{\rm rh}$ [Myr]
LM1	0.58	10k	2, 4, 6, 7	0.0, 0.6, 1.2, 1.8	1.030
LM2	0.58	25k	2, 4, 6, 7	0.0, 0.6, 1.2, 1.8	1.466
MM	10	10k	2, 4, 6, 7	0.0, 0.6, 1.2, 1.8	0.248
HM	50	10k	2, 4, 6, 7	0.0, 0.6, 1.2, 1.8	0.110

Table 3.3.3: Subset of cluster models used for direct comparison of rotational effects. The restriction to $W_0 = \{2, 4, 6, 7\}$ ensures a consistent parameter space across all values of the rotation parameter ω_0.

concentrations $W_0 = \{2, 4, 6, 7\}$ presented in Table 3.3.2. This is then reflected in Table 3.3.3, which is the rotational analog of Table 3.3.2. Higher-concentration non-rotating models are retained and discussed separately when addressing the dependence on cluster concentration alone.

The number of particles, N, depends on the adopted mass set. Low-mass (LM) clusters are simulated with $N = 10\,\mathrm{k}$, $25\,\mathrm{k}$ and $50\,\mathrm{k}$, denoted as LM1, LM2 and LM3 respectively, in order to assess numerical convergence. Similarly, for the non-rotating mid-mass models, simulations with $N = 10\,\mathrm{k}$ and $25\,\mathrm{k}$ are referred to as MM1 and MM2. In contrast, rotating mid-mass models are limited to $N = 10\,\mathrm{k}$ and are therefore denoted simply as MM, as no rotational simulations with $N = 25\,\mathrm{k}$ were performed for this mass set. High-mass models are restricted to $N = 10\,\mathrm{k}$ owing to their shorter evolutionary timescales and higher computational cost.

All clusters share a common initial half-mass radius of $r_{\rm hm} = 0.1\,\mathrm{pc}$ and are evolved for $15\,\mathrm{Myr}$. Each simulation represents a single stochastic realization for a given parameter combination. Stars that become unbound are removed once

they exceed the standard escape criterion of NBODY6++GPU, corresponding to several times the virial radius.

The final range of parameters defining the simulated rotating cluster models, including the stellar mean mass $m_\star$, particle number N, concentration W_0 (see Section 2.4.3), rotation ω_0, and initial half-mass relaxation time $t_{\rm rh}$, are summarized in Table 3.3.3. The rotation parameter ω_0 is defined following the rotating King model introduced in Section 2.4.4 (Eq. (2.4.15)), while the initial half-mass relaxation time $t_{\rm rh}$ is computed as described in Section 2.2.3 (Eq. (2.2.7)).

3.4 Initial conditions

Figure 3.4.1 illustrates the projected initial particle phase-space distributions constructed in static equilibrium, for the adopted rotating cluster models at fixed concentration $W_0 = 7$ and particle number $N = 50{,}000$, for increasing values of the dimensionless rotation parameter ω_0. The non-rotating reference configuration ($\omega_0 = 0.0$) was generated using MCLUSTER, while the rotating models were constructed with FOPAX. For visualization purposes, particles are shown in projected configuration space (x, y) and color-coded by their line-of-sight velocity component, using a common color scale to allow direct comparison between models. All snapshots have been rescaled to a common half-mass radius of $r_{\rm hm} = 0.1\,\mathrm{pc}$ and expressed in physical units. Although the quantitative analysis presented throughout this work is primarily based on lower-resolution simulations, the higher-resolution models displayed here are used exclusively for visualization, as they more clearly reveal the underlying spatial and kinematic structure. As the rotation parameter increases, the systems display increasing flattening and a progressively stronger velocity gradient across the cluster, reflecting the growing contribution of ordered rotation and global angular momentum in the initial conditions.

All clusters satisfy the virial equilibrium condition with a virial ratio of $Q = T/|V| = 0.5$ prior to the start of the simulations. The equilibrium realizations were first constructed in physical units and subsequently converted to NBODY units, where $G = M = -4E = 1$. This conversion is performed internally by NBODY6++GPU and is controlled by the main input parameters, which define the physical scaling of the virial radius and the mean stellar mass. In NBODY units, the total cluster mass is normalized to unity, and in equal-mass systems

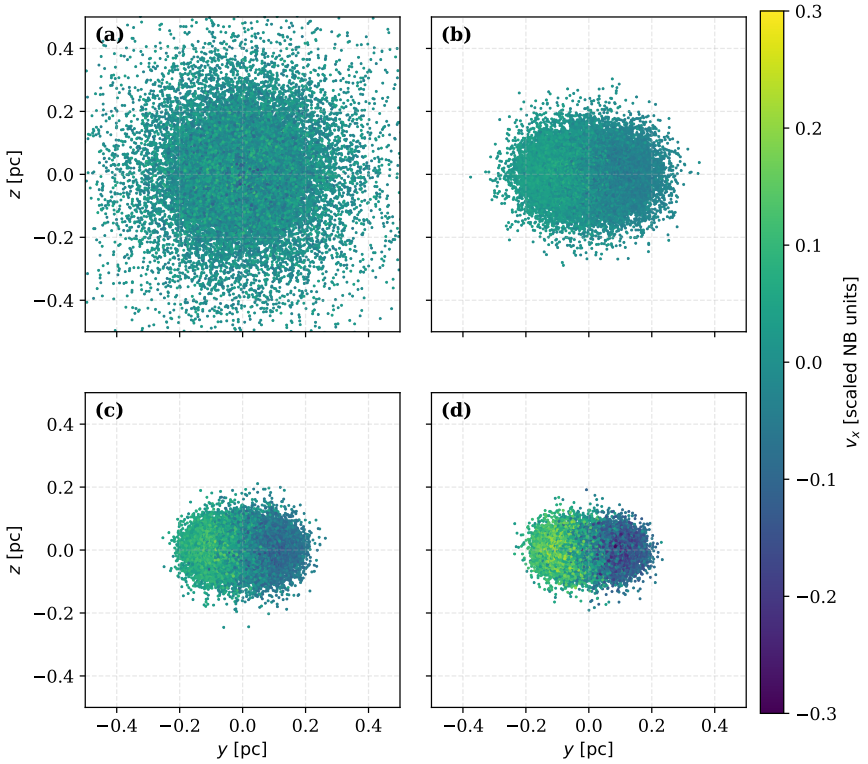

Figure 3.4.1: Initial projected phase-space distributions of equilibrium star cluster models with concentration parameter $W_0 = 7$ and particle number $N = 50{,}000$, shown for different values of the rotation parameter ω_0. Panels **(a)**–**(d)** correspond to $\omega_0 = 0.0$, 0.6, 1.2, and 1.8, respectively. Particles are shown in the projected (x, y) plane and color-coded by their line-of-sight velocity component using a common color scale. All models have been rescaled to a half-mass radius of $r_{\rm hm} = 0.1\,{\rm pc}$.

each particle initially has a mass of $1/N$. For all models considered in this work, the scaling was chosen such that the initial physical half-mass radius is fixed to $r_{\rm hm} = 0.1\,\mathrm{pc}$, independent of concentration or rotation.

The non-rotating King models generated with MCLUSTER are provided directly in standard N-body units, while the rotating configurations produced with FOPAX require a preliminary conversion before being imported. In both cases, NBODY6++GPU internally rescales the input configurations to its working unit system prior to integration, ensuring a consistent numerical treatment across models with different concentrations, rotation parameters, and particle numbers. The phase-space structure of the equilibrium configurations is therefore preserved at the onset of the N-body evolution.

Each particle in the external initial conditions corresponds to a single star, with its mass, three-dimensional position, and velocity fully specified. All simulations start from initially equal-mass, single-star systems, with no primordial binaries and no residual gas component. As a consequence, processes associated with gas accretion or dynamical friction from a gaseous background are absent. The clusters are evolved as isolated, self-gravitating systems, in the absence of any external tidal field or galactic potential. Stars that become unbound during the evolution are identified dynamically and classified as escapers once they move beyond the characteristic escape radius adopted by the code.

The influence of rotation on the initial structural properties of the clusters is quantified in Table 3.4.1, which summarizes the core radius, core particle number, and core number density for the low-mass model subset. As discussed above, rotation significantly modifies the internal structure of the cluster core, with higher rotation parameters leading to larger core radii, higher core particle numbers, and lower core densities at fixed concentration. These systematic differences in the initial conditions provide the baseline for the subsequent dynamical evolution analyzed in the following sections.

The rotating cluster models exhibit a clear increase in core rotational support with increasing values of the dimensionless rotation parameter ω_0. In particular, the characteristic core rotational velocity approximately follows the relative scaling of $\omega_0 = \{0.6, 1.2, 1.8\}$, indicating that the imposed rotation parameter effectively controls the degree of ordered motion within the cluster core. This behavior is

further reflected in the mean absolute rotational velocity averaged over Lagrangian radii, which shows a consistent trend among rotating models, while non-rotating clusters display a more isotropic velocity distribution with no coherent rotational pattern.

Low-mass models (LM) Number of particles = 10000				
W_0	ω_0	$r_{\mathrm{c},0}$ [pc]	$N_{r_{\mathrm{c},0}}$	$\eta_{r_{\mathrm{c},0}}$ [$\times 10^6$ N/pc^3]
2	0.0	0.0544	1513	2.24
	0.6	0.0570	1653	2.13
	1.2	0.0593	1737	1.98
	1.8	0.0631	1921	1.82
4	0.0	0.0472	1289	2.93
	0.6	0.0503	1420	2.66
	1.2	0.0602	1801	1.97
	1.8	0.0736	2444	1.46
6	0.0	0.0321	875	6.34
	0.6	0.0421	1159	3.71
	1.2	0.0658	2090	1.75
	1.8	0.0810	2879	1.30
7	0.0	0.0216	590	14.02
	0.6	0.0380	1057	4.60
	1.2	0.0698	2304	1.62
	1.8	0.0824	2943	1.26

Table 3.4.1: Initial core radius $r_{\mathrm{c},0}$, number of particles within the core $N_{r_{\mathrm{c},0}}$, and corresponding core number density $\eta_{r_{\mathrm{c},0}}$ for the low-mass cluster models, listed as a function of the concentration parameter W_0 and the dimensionless rotation parameter ω_0. All quantities are measured at the start of the simulations.

Table 3.4.1 summarizes the initial core properties for the low-mass model subset, including the initial core radius $r_{\mathrm{c},0}$, the number of particles within the core $N_{r_{\mathrm{c},0}}$, and the corresponding core number density $\eta_{r_{\mathrm{c},0}}$. For a fixed concentration W_0, models with higher rotation parameters systematically contain a larger number of particles within the core radius, reflecting the redistribution of mass driven by rotational support. The magnitude of this effect depends strongly on the concentration of the model.

For non-rotating and weakly rotating clusters ($\omega_0 = 0.0$ and 0.6), increasing the concentration parameter W_0 leads to a reduction in the number of particles contained within the core, consistent with the expected decrease in core radius for more centrally concentrated King models. In contrast, models with stronger

rotation ($\omega_0 = 1.2$ and 1.8) exhibit the opposite trend: despite the increase in concentration, both the core radius and the number of core particles increase, indicating that rotation counteracts the effect of concentration. As a result, the difference in core particle number between low- and high-rotation models becomes more pronounced at higher concentrations.

Despite the increase in the number of particles within the core at higher rotation, the core number density decreases systematically with increasing ω_0 for a given concentration as $\rho_c \propto N_{r_c}/r_c^3$, thus the growth of the core radius overcomes the increase of the number of enclosed particles.

3.5 The NBODY6++GPU main input

The main input file of NBODY6++GPU defines the global numerical setup of each simulation. It specifies the total integration time, timestep accuracy parameters for both regular and irregular forces, the output frequency and diagnostics, as well as the suite of control flags collectively known as `KZ` parameters. Through these settings, the user controls the physical modules to be activated—such as stellar evolution, collisions, or external tidal fields—and the precision and cadence of the integration.

Although NBODY6++GPU includes internal routines to generate initial particle distributions (for example, Plummer or uniform-density models; Plummer 1911), these capabilities are not used in the present work. Instead, all simulations rely on externally generated equilibrium King models, both rotating and non-rotating, as described in the previous subsection.

All simulations presented here adopt these settings to ensure consistent normalization, unit conversion, and integration control across the entire model grid. Together with the equilibrium initial conditions, this configuration guarantees reproducible, dynamically consistent realizations for all clusters prior to their evolution.

3.6 Data output analysis

The simulation outputs were post-processed to extract a series of global and structural diagnostics that trace the dynamical evolution of the clusters. These

quantities allow the comparison of models with different initial concentrations, rotation parameters, and stellar masses, and provide a direct link between the internal dynamics and the formation of compact remnants. The primary diagnostics analyzed in this work include the number of stellar collisions, the number of escapers, the evolution of the Lagrangian radii, and the black hole (BH) mass fraction over time.

Collisions. In NBODY6++GPU collisions between individual stars are recorded directly whenever two stellar components merge or experience a physical contact within the adopted collision criterion. Each event stores the identities and properties of the participating stars, allowing the total number of collisions to be tracked as a function of time. This quantity provides a direct measure of the collisional activity of the system and serves as an indicator of the cluster's approach to the runaway regime that may lead to the formation of a massive merger product.

Escapers. Stars that acquire positive total energy and move beyond 20 times the scale radius are no longer gravitationally bound by the cluster. Their cumulative number and escape rate are obtained from the corresponding diagnostic files. The evolution of the escaper population reflects the balance between two-body relaxation, mass loss, and provides a measure of cluster evaporation efficiency even in the absence of an external tidal field.

Lagrangian radii. The structural evolution of the clusters is characterized through their Lagrangian radii, defined as the three-dimensional radii enclosing fixed mass fractions of the bound cluster mass (e.g., 5%, 10%, 20%, 50%, and 90%). Among these, the radius enclosing 50% of the total mass corresponds to the half-mass radius $r_{\rm hm}$, a standard indicator of the cluster's overall size. The time evolution of the inner Lagrangian shells traces the progressive contraction of the core, while the outer shells describe the expansion of the halo. Together, these radii provide a direct, model-independent probe of the structural response of the system to relaxation, rotation, and mass loss.

Black hole efficiency. The efficiency of black hole formation is quantified through the time evolution of the most massive object (MMO) in each cluster,

which serves as a proxy for the potential runaway collision product. The instantaneous efficiency, denoted as $\epsilon_{\rm BH}$, is defined as the ratio between the mass of the MMO, $M_{\rm MMO}(t)$, and the initial total stellar mass of the cluster. Although this quantity is referred to as a "BH efficiency," the MMO does not necessarily collapse into a black hole within the simulated time, as rejuvenation following repeated mergers can delay or prevent its final collapse under the adopted stellar evolution prescriptions (see Section 3.2).

To avoid counting low-mass merger remnants that are unlikely to produce a black hole, $\epsilon_{\rm BH}$ is set to zero whenever $M_{\rm MMO} < 20\,M_\odot$ or $M_{\rm MMO} < 5\,m_\star$ at the end of the simulation, where $m_\star$ is the initial mean stellar mass. These thresholds are adopted as pragmatic limits to exclude minor mergers or stochastic fluctuations that do not represent genuine runaway growth. The evolution of $\epsilon_{\rm BH}$ thus indicates that a fraction of the mass of the cluster that will become part of the central massive object and will later be compared to the theoretical critical mass thresholds introduced in Section 2.3.4.

Finally, the total number of collisions and escapers attained by each model after 15 Myr, as well as the dependence of the BH efficiency on the initial concentration W_0 and stellar mass set, are presented and discussed in detail in Chapter 4. These quantities serve as the main empirical outputs linking the numerical results to the theoretical predictions of cluster core collapse and BH seed formation.

Chapter 4

Results

This chapter presents the main results obtained from the numerical simulations of dense stellar clusters described in the previous sections. The analysis focuses on the dynamical and structural evolution of the systems over the first 15 Myr, with particular emphasis on the role of initial concentration, rotation, stellar mass, and particle number. Key diagnostics include the evolution of Lagrangian radii, stellar collision rates, the production of escapers and mass loss, and the growth of the most massive object formed through successive collisions. The results are presented by progressively moving from a global overview of the parameter space to a detailed examination of the physical processes governing core contraction, collisional activity, and the final cluster state.

4.1 Global overview

All cluster models were evolved for a fixed physical time of 15 Myr, independent of the adopted stellar mass, particle number, initial concentration, or rotation parameter. Across the explored parameter space, the simulations exhibit a wide range of dynamical behaviors, reflecting the strong sensitivity of dense stellar systems to their initial conditions.

Figure 4.0.1 presents a global overview of the main evolutionary channels examined in this work, using a representative low-mass, non-rotating cluster model as a reference case. By combining collisional activity, black hole formation efficiency, mass loss through escapers, and structural evolution within a single multi-panel

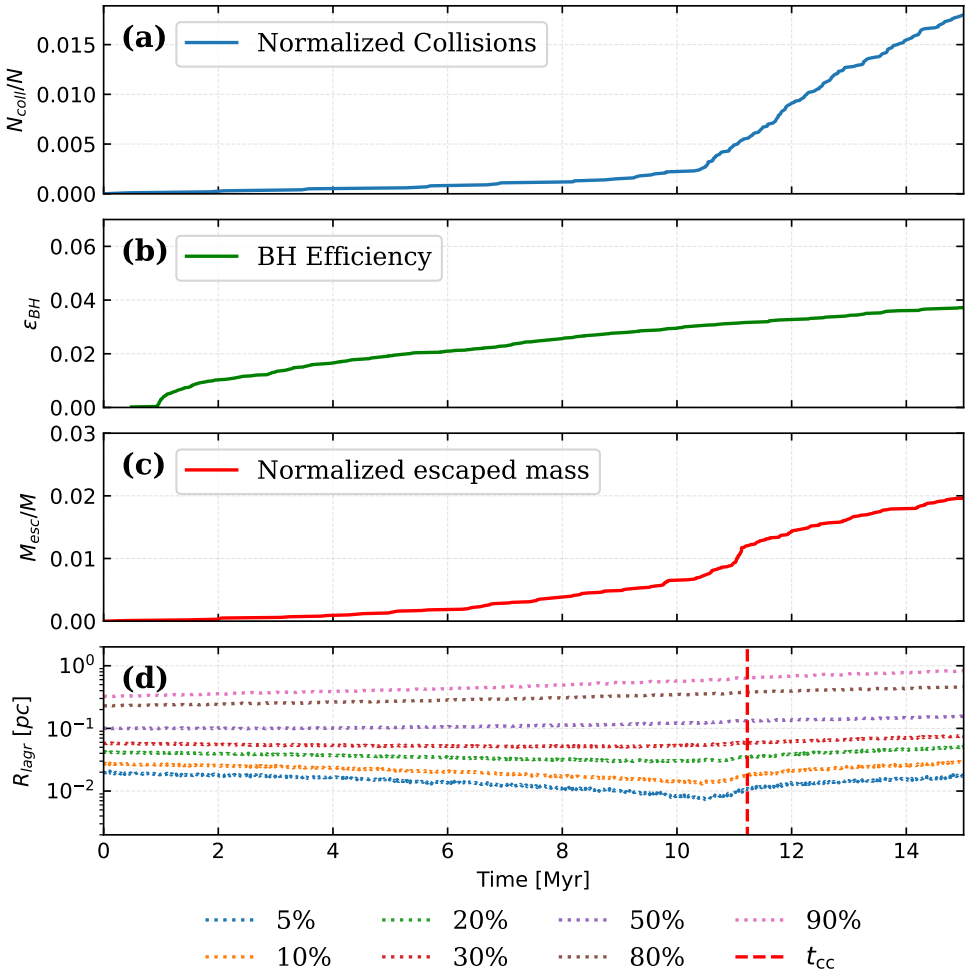

Figure 4.0.1: Global overview of the early dynamical, structural, and collisional evolution of the reference low-mass model LM1 ($N = 10\,\mathrm{k}$, $\langle m \rangle = 0.58\,M_\odot$), with initial concentration $W_0 = 7$ and no rotation ($\omega_0 = 0.0$). From top to bottom, the panels show: **(a)** the cumulative number of stellar collisions normalized by the initial number of stars, N_{coll}/N; **(b)** the black hole formation efficiency ϵ_{BH}; **(c)** the total mass lost through escapers, normalized by the initial cluster mass, M_{esc}/M; and **(d)** the time evolution of the Lagrangian radii, illustrating the internal structural evolution of the cluster. In the bottom panel, the vertical dashed line marks the estimated time of core collapse t_{cc}, computed from the initial half-mass relaxation time following the scaling of Quinlan (1996). This figure provides a compact summary of the coupled evolution of collisions, compact-object formation, mass loss, and core contraction that is explored in detail throughout the Results section.

diagram, this figure provides a coherent framework for interpreting the detailed results discussed in the following sections.

The top panel illustrates the cumulative growth of stellar collisions, highlighting the early dynamical phase during which collisional processes are most efficient. The second panel traces the build-up of a compact remnants through the black hole formation efficiency, linking stellar evolution to the dynamical state of the cluster. The third panel quantifies the progressive loss of mass via escapers, reflecting the combined effects of two-body relaxation, mass segregation, and dynamical heating. Finally, the bottom panel shows the evolution of the Lagrangian radii, providing a direct view of the internal structural response of the system and the contraction of the central regions toward core collapse.

The vertical marker in the Lagrangian-radii panel indicates the estimated core-collapse time, which serves as a useful reference for connecting structural evolution with the timing of enhanced collisional activity and compact-object formation. Together, these diagnostics summarize the coupled dynamical and evolutionary processes that govern the early evolution of dense stellar clusters and motivate the more detailed, parameter-dependent analysis presented below.

Figure 4.1.1 provides an overview of the cumulative collisional activity across the full set of non-rotating cluster models. The figure shows the total number of stellar collisions accumulated up to a given time t_H, normalized by the total number of stars, as a function of the initial concentration parameter W_0. Panels **(a)** through **(d)** present snapshots at $t_H = 1$, 5, 10, and 15 Myr, respectively, allowing the time dependence of the collisional buildup to be assessed. Low-, mid-, and high-mass models are distinguished by color, while different particle numbers are indicated by marker style. This representation enables a direct comparison of how stellar mass scale and central concentration jointly influence the efficiency and timing of collisional processes during the early evolution.

A first robust trend is the strong dependence of the early collisional activity on the initial King concentration. Models with low central concentration generally exhibit delayed or suppressed collisional evolution compared to their more concentrated counterparts. This effect is particularly pronounced in the low-mass (LM) set, where several low-concentration models ($W_0 < 7$) do not form a significantly massive central object (defined here as having $M_{\rm MMO} > 20\,M_\odot$) within the

simulated time-span.

The mid-mass (MM) and high-mass (HM) models exhibit substantially enhanced collisional activity compared to their low-mass counterparts. In the HM set, stellar collisions are concentrated predominantly in the early stages of the evolution, with the collision rate declining sharply at approximately 5 Myr. As a result, despite experiencing a higher collision rate at early times, HM models accumulate by 15 Myr a total number of collisions comparable to that of the MM models, as shown in Figure 4.1.1.

Across all mass sets, the number of escapers remains modest during the early evolution and increased as the systems dynamically evolved. In general, models with a larger number of particles tend to retain a higher fraction of bound stars, leading to a reduced total number of escapers. An exception to this trend is found in the most rapidly rotating models ($\omega_0 = 1.8$), which consistently exhibit enhanced mass loss through escapers.

These global trends provide the context for the more detailed analysis presented in the following sections, where the early structural evolution, the onset of the collisional regime, and the growth of central massive objects are examined in detail.

4.2 Early dynamical and structural evolution

Models with lower central concentration exhibit a comparatively quiescent early evolution, characterized by a reduced number of stellar collisions and a smaller fraction of escaping mass when compared to higher-concentration systems. Over the first $\sim$ 15 Myr, the simulated clusters can be broadly classified using the Quinlan core-collapse timescale (Quinlan, 1996) as a reference criterion.

Systems whose estimated core-collapse timescale is comparable to or longer than the duration of the simulation exhibit only mild structural evolution during this early phase. These low-concentration models maintain a low collision rate throughout the integration, as shown in Figure 4.1.1, and display little to no contraction of their Lagrangian radii, as discussed below.

Figure 4.2.1 illustrates the early structural evolution of selected non-rotating King models through the time evolution of their Lagrangian radii. Each panel

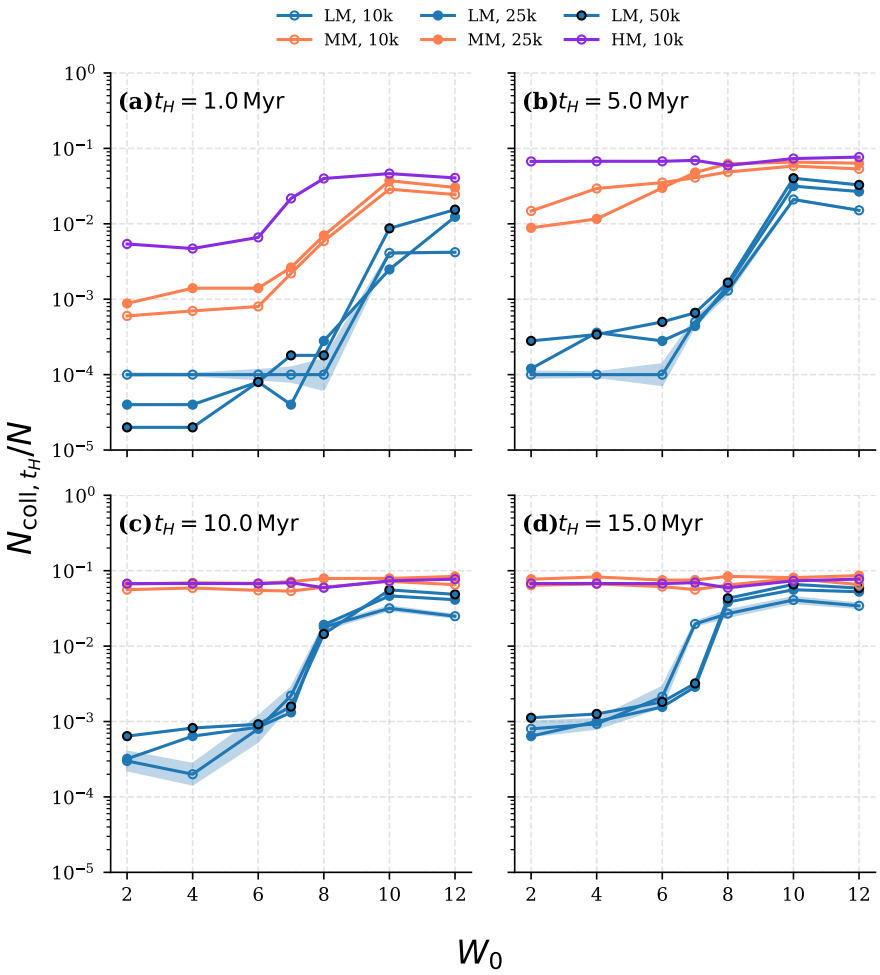

Figure 4.1.1: Total number of stellar collisions accumulated up to time t_H, normalized by the total number of stars ($N_{\rm coll}/N$), as a function of the initial cluster concentration W_0 for non-rotating models. Panels **(a)**–**(d)** show snapshots at $t_H = 1$, 5, 10, and 15 Myr, respectively. Low-mass (LM), mid-mass (MM), and high-mass (HM) models are distinguished by color, while different particle numbers are indicated by marker style (see legend). High-mass models exhibit an early saturation of collisional activity, reaching a nearly concentration-independent plateau by $\sim$ 5 Myr. In contrast, MM models show a progressive increase in collisions with time, approaching the HM level by $t_H \gtrsim 10$ Myr, particularly at higher concentrations. This figure illustrates how stellar mass scale and concentration jointly regulate the timing and efficiency of collisional processes.

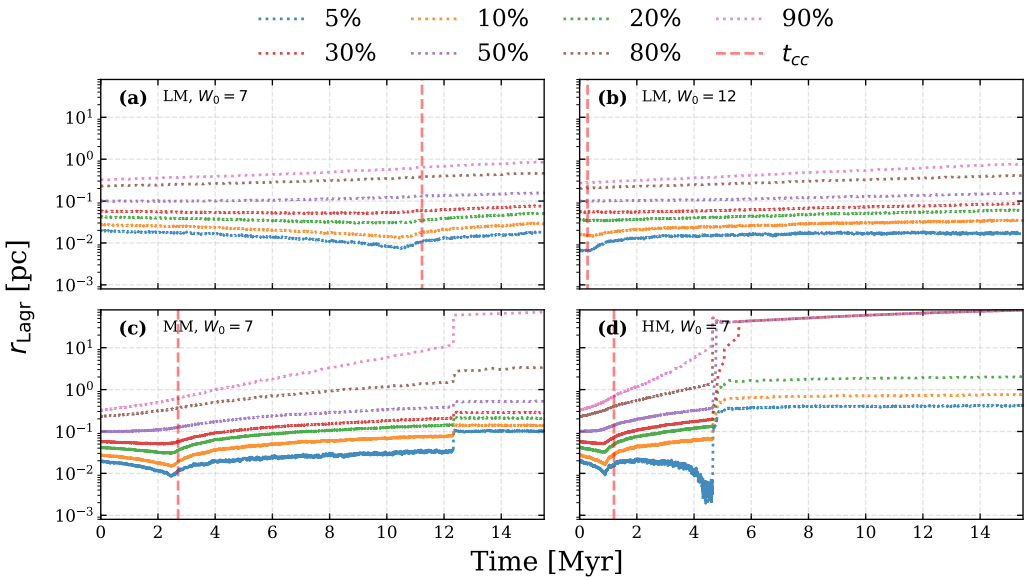

Figure 4.2.1: Time evolution of the Lagrangian radii for selected non-rotating King models ($\omega_0 = 0$), illustrating the early structural response as a function of concentration and stellar mass scale. Panels **(a)**, **(c)**, and **(d)** correspond to low-mass (LM), mid-mass (MM), and high-mass (HM) models with $W_0 = 7$, respectively, while panel **(b)** shows an LM model with higher concentration, $W_0 = 12$. Vertical markers indicate the estimated core-collapse time $t_{\rm cc}$, obtained from the initial half-mass relaxation time and the concentration-dependent scaling of Quinlan (1996) (see Table 2.5.1). In all cases, the estimated $t_{\rm cc}$ coincides approximately with the contraction of the innermost (5%) Lagrangian radii. MM and HM models exhibit an abrupt global expansion at $\sim 10\,$Myr and $\sim 5\,$Myr, respectively.

shows the fractional mass radii enclosing fixed percentages of the total cluster mass, allowing the degree of core contraction and global expansion to be tracked as a function of time. Panels **(a)**, **(c)**, and **(d)** correspond to low-, mid-, and high-mass models with identical concentration ($W_0 = 7$), while panel **(b)** presents a more centrally concentrated low-mass model with $W_0 = 12$, highlighting the effect of concentration at fixed mass scale. Vertical markers indicate the estimated core-collapse time $t_{\rm cc}$, computed from the initial half-mass relaxation time using the concentration-dependent scaling of Quinlan (1996) (see Table 2.5.1). This figure therefore provides a direct diagnostic of the early dynamical response of the cluster and the onset of core collapse across different mass and concentration regimes.

Clusters with higher central concentration evolve much more rapidly. In particular, models with $W_0 = 10$ and, more prominently, $W_0 = 12$ exhibit an elevated initial collision rate and undergo a rapid early contraction, as indicated by the inward evolution of their innermost Lagrangian radii (Figure 4.2.1). In these systems, multiple stellar collisions occur within a relatively short time interval, signaling the development of a dynamically active and increasingly dense core.

The dependence on the stellar mass spectrum further modulates the early evolution. Although the total cluster mass is set by the product $M = Nm_\star$, models with similar M but different combinations of particle number N and mean stellar mass $m_\star$ are expected to evolve differently (Reinoso et al., 2018, 2020; Vergara et al., 2022). This effect is further amplified when concentration is taken into account. Medium- and high-mass models, characterized by larger mean stellar masses, exhibit a more rapid onset of core contraction, consistent with their shorter relaxation times and enhanced collisional cross sections.

In the high-mass set, this accelerated contraction phase is abruptly interrupted at $t \simeq 5\,\mathrm{Myr}$ by a simultaneous expansion affecting all Lagrangian radii (Figure 4.2.1). Such a global response may result either from the collapse of a single, rapidly growing massive object or from the near-simultaneous collapse of multiple massive stars, temporarily reversing the core contraction and driving the observed expansion.

Stellar evolution also influences the evolution of the mid-mass models. In several cases, the contraction phase is halted at later times than in the high-mass set,

typically between $\sim$ 10 and 15 Myr. This interruption is followed by a rapid global expansion of all Lagrangian radii, marking the end of the collapse phase. Although delayed relative to the high-mass models, this behaviour suggests that stellar evolution can similarly regulate the post-collapse response of medium-mass clusters. This overall highlights the role of stellar evolution in regulating the early dynamical evolution of massive clusters.

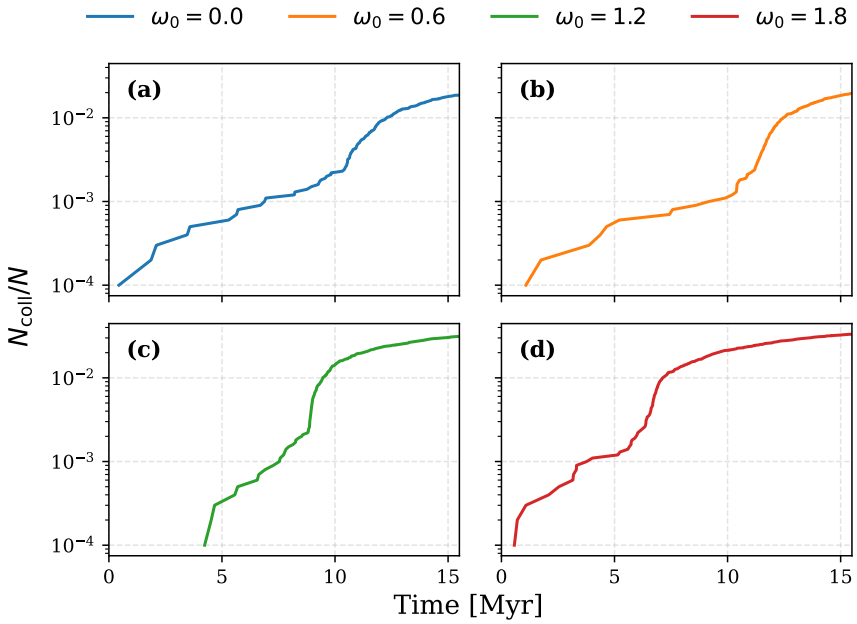

Figure 4.2.2: Time evolution of the cumulative number of stellar collisions for rotating star cluster models with $N = 10^4$, $W_0 = 7$ and mean stellar mass $\langle m \rangle = 0.58, M_\odot$. Panels **(a)**–**(d)** correspond to rotation parameters $\omega_0 = 0.0$, 0.6, 1.2, and 1.8, respectively. Solid lines denote the cumulative number of collisions as a function of time for each rotation model. The models and physical scaling are identical to those presented in Figure 4.2.3.

4.3 Core contraction and collisions

Figures 4.2.1 and 4.2.3 illustrate the structural evolution of the clusters, while Figure 4.2.2 traces the associated collisional activity for models sharing the same stellar mass and particle number but differing in their degree of rotational support. The evolution of the innermost Lagrangian radii provides a direct diagnostic of core contraction, whereas the cumulative number of stellar collisions reflects the development of a dense and dynamically active central region.

The impact of rotation on the early dynamical evolution is examined through the

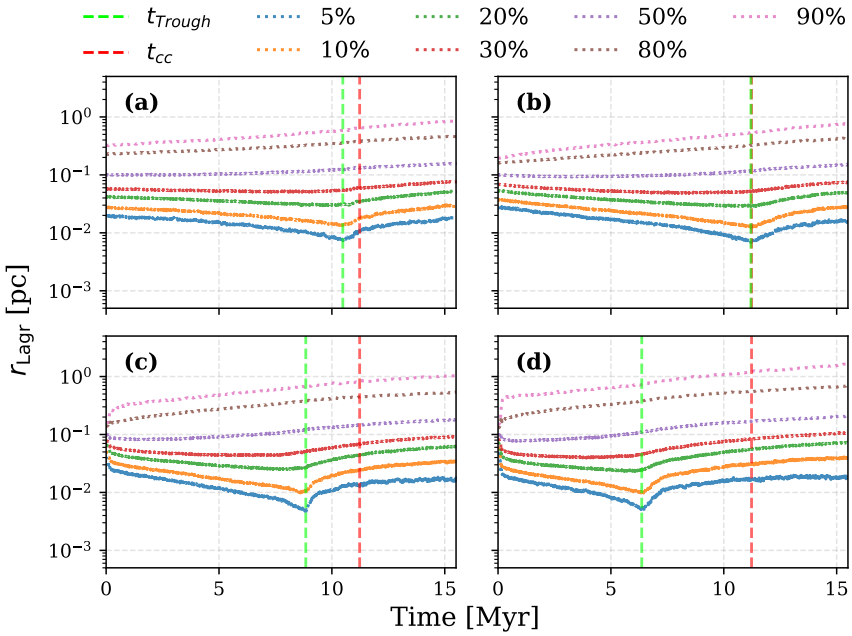

Figure 4.2.3: Time evolution of the Lagrangian radii for rotating star cluster models with $N = 10^4$, $W_0 = 7$ and $\langle m \rangle = 0.58\,M_\odot$. Panels **(a)**–**(d)** correspond to rotation parameters $\omega_0 = 0.0$, 0.6, 1.2, and 1.8, respectively. Dotted lines indicate radii enclosing 5%, 10%, 20%, 30%, 50%, 80%, and 90% of the cluster mass. The red dashed vertical line marks the estimated core-collapse time $t_{\rm cc}$ derived from the non-rotating scaling of Quinlan (1996), while the green dashed line indicates the actual onset of core contraction, identified from the minimum of the 5% Lagrangian radius. The comparison highlights the tendency of rotating models to undergo core contraction earlier than predicted by non-rotating estimates.

coupled evolution of collisional activity and internal structure for a representative set of rotating models. Figures 4.2.2 and 4.2.3 present, respectively, the cumulative number of stellar collisions and the time evolution of the Lagrangian radii for clusters with identical mass, particle number, and concentration, differing only in their initial degree of rotational support.

Figure 4.2.2 shows that increasing rotational support leads to an earlier onset of collisional activity. Models with higher ω_0 exhibit a more rapid initial increase in the cumulative number of stellar collisions, indicating that collisions begin at earlier times compared to the non-rotating case. This behavior suggests that rotation promotes an early phase of enhanced central density, accelerating the conditions required for stellar collisions despite the presence of angular momentum support.

Figure 4.2.3 further demonstrates that the onset of core contraction occurs systematically earlier in rotating models. While the red dashed line marks the core-collapse time estimated from the non-rotating scaling relation of Quinlan (1996), the actual contraction of the innermost 5% Lagrangian radius, indicated by the green dashed line, precedes this estimate increasingly as the rotation parameter ω_0 increases. This offset highlights the limitations of applying non-rotating core-collapse prescriptions to rotating systems and indicates that angular momentum alters the early dynamical pathway toward core collapse.

As the rotation parameter ω_0 increases, the onset of central contraction occurs systematically earlier, as indicated by the more rapid inward migration of the 5% and 10% Lagrangian radii. This accelerated contraction is closely followed by a sharp increase in the collision rate, demonstrating a strong temporal coupling between structural collapse and collisional activity. The enhanced collision rates observed in rotating models are therefore a direct consequence of the higher central densities achieved during the early phases of evolution.

The dependence of collisional activity on stellar mass scale and particle number is illustrated in Figure 4.3.1, which compares normalized collision-rate histograms for non-rotating models with identical concentration ($W_0 = 7$) and rotation (ω_0). Collisions are binned in units of the initial half-mass relaxation time of the reference low-mass model (LM1), allowing the temporal distribution of collisions to be compared on a common dynamical timescale. In the low-mass regime, the

two models exhibit qualitatively different behavior depending on particle number. For the LM1 case, collisional activity remains modest over several relaxation times, with a clear enhancement in the bin closest to the estimated epoch of core collapse. In contrast, for the LM2 model the predicted core-collapse time occurs near the end of the simulation, and the final relaxation-time bin spans a shorter physical interval than the preceding ones. This highlight how models models with relaxation times comparable to or longer than the total integration time naturally display a reduced number of recorded collisions within the simulated window.

In contrast, the mid-mass and high-mass models undergo an early, intense phase of collisional activity followed by a rapid truncation, i.e. these models show that the majority of collisions occur within the first few bins, with no further collisions recorded at later times. This behavior is driven by stellar evolution: once the most massive stars undergo compact-object formation, the resulting decrease in stellar radii and collisional cross-sections leads to a sharp decline in collision rates, effectively halting further collisional phase. The presence of empty late-time bins in panels **(c)** and **(d)** therefore reflects a genuine physical cessation of collisional activity.

The internal evolution of the cluster core is further quantified in Figure 4.3.2, which traces the time evolution of key core properties summarized in Table 3.4.1 for a representative low-mass, non-rotating model (LM1; $N = 10\,\mathrm{k}$, $W_0 = 7$, $\omega_0 = 0.0$). As the core radius contracts, the number of particles enclosed within the core decreases; however, the reduction in r_c dominates the evolution. As a result, the core number density increases rapidly by several orders of magnitude, marking the onset of core collapse and the transition to a high-density regime.

A complementary view of the core evolution is provided in Figure 4.3.3, which relates the core number density η_{r_c} directly to the core radius r_c for the same reference model. Unlike the time-series representation shown in Figure 4.3.2, this diagram offers a time-independent diagnostic that highlights the structural pathway followed by the core during contraction.

As the core radius decreases, the number density increases by several orders of magnitude, reflecting the rapid concentration of particles into an increasingly compact central region. The inverted horizontal axis emphasizes this progression toward smaller spatial scales, making explicit the strong, non-linear coupling

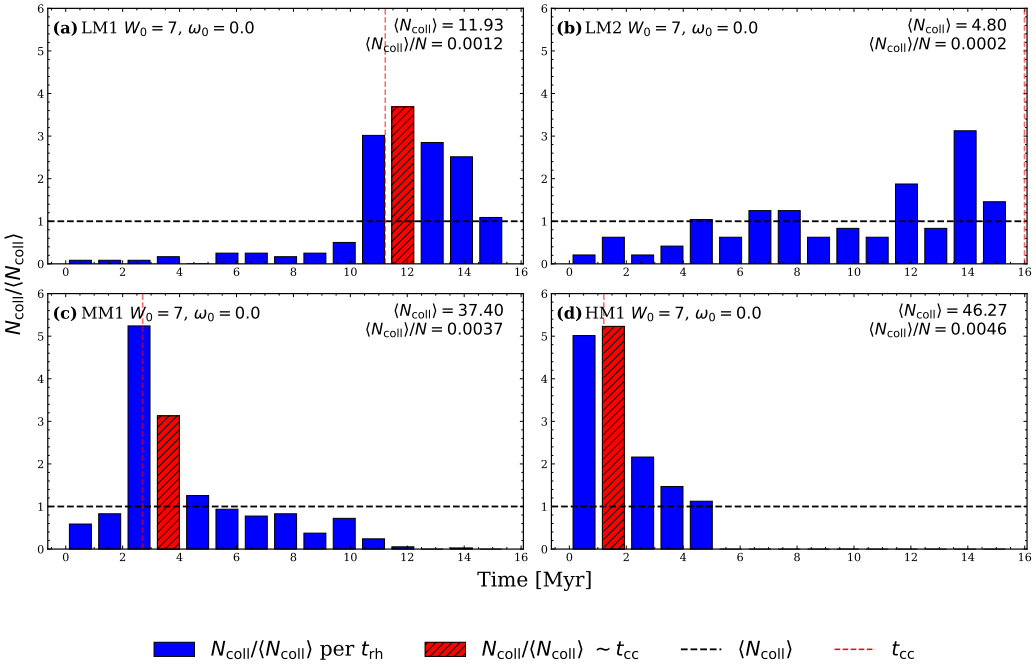

Figure 4.3.1: Normalized histograms of stellar collisions for cluster models with fixed concentration $W_0 = 7$ and no initial rotation ($\omega_0 = 0.0$), comparing different stellar mass regimes and particle numbers. The height of each bin corresponds to the number of collisions occurring within that time interval, normalized by the mean number of collisions per bin for each model. Time is binned in units of the initial half-mass relaxation time $t_{\rm rh}$ of the low-mass $N = 10\,\mathrm{k}$ model shown in panel **(a)**, expressed in Myr, such that each bin represents one relaxation-time interval on a common temporal scale. Panels **(a)** and **(b)** show the low-mass models LM1 ($N = 10\,\mathrm{k}$) and LM2 ($N = 25\,\mathrm{k}$), with total initial masses of $5.8 \times 10^3\,M_\odot$ and $1.58 \times 10^4\,M_\odot$, respectively. Panels **(c)** and **(d)** correspond to the mid-mass ($m_\star = 10\,M_\odot$) and high-mass ($m_\star = 50\,M_\odot$) models with $N = 10\,\mathrm{k}$. In the mid- and high-mass cases, stellar evolution leads to an early termination of the collisional phase, resulting in empty bins at later times. The horizontal black dashed line marks the normalized mean collision rate (unity by construction), while the vertical red dashed line indicates the estimated core-collapse time (Table 2.5.1). The hatched red bin highlights the relaxation-time interval closest to the predicted core-collapse epoch.

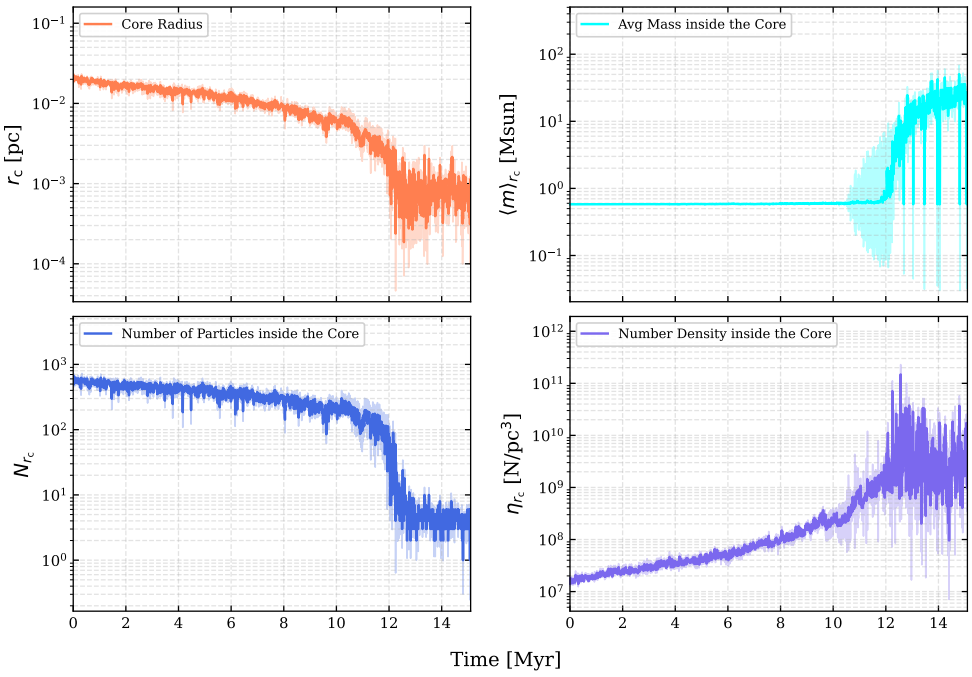

Figure 4.3.2: Time evolution of core properties for the reference low-mass model LM1 ($N = 10\,\mathrm{k}$, $m_\star = 0.58\,M_\odot$) with concentration $W_0 = 7$ and no initial rotation ($\omega_0 = 0.0$). The top-left panel shows the core radius r_c, the top-right panel the mean stellar mass enclosed within the core, the bottom-left panel the number of particles inside the core radius, and the bottom-right panel the corresponding core number density η_{r_c}. As the core contracts, the number of particles decreases moderately; however, the rapid reduction in r_c dominates the evolution, producing a steep increase in the core number density by several orders of magnitude relative to its initial value. This behavior reflects the onset of gravothermal contraction and the development of a dense, collisionally active core.

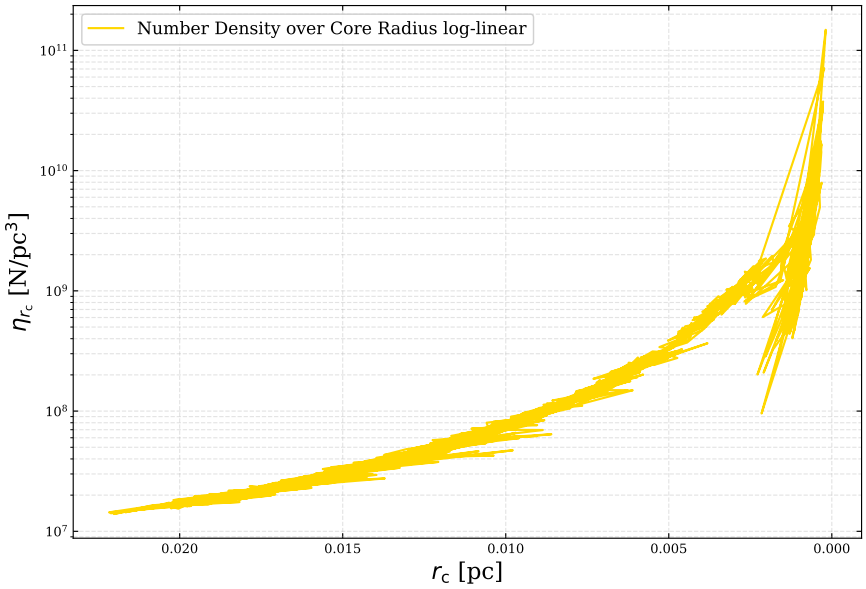

Figure 4.3.3: Core number density η_{r_c} as a function of the core radius r_c for the representative low-mass model LM1 ($N = 10\,\mathrm{k}$, $W_0 = 7$, $\omega_0 = 0.0$). The horizontal axis is inverted to emphasize the physical progression toward smaller core sizes, highlighting the rapid increase in central density as the core contracts. As r_c decreases, the core number density rises by several orders of magnitude, tracing the transition from a diffuse central configuration to a compact, high-density core. This diagram provides a time-independent representation of the core evolution and is complementary to the time-series diagnostics shown in Figure 4.3.2. The trajectory toward small r_c and high η_{r_c} identifies the onset of core collapse and the development of a dense, dynamically active central region.

between r_c and η_{r_c}. The trajectory toward low r_c and high η_{r_c} identifies the onset of core collapse and marks the transition from a diffuse core to a dense, collisionally active state.

4.4 Growth of the central massive object

By tracking the accumulation of mass through successive merger events, this analysis provides a direct characterization of the collisional growth phase that follows the onset of core contraction and precedes the later dynamical evolution of the system.

Figure 4.4.1 shows the temporal evolution of the black hole formation efficiency for clusters that share identical structural and dynamical parameters but differ in their mean stellar mass. For all models, $\epsilon_{\rm BH}$ increases in discrete steps associated with successive collisions involving the most massive object, reflecting its growth through collisional mergers. The impact of mass loss processes on the MMO is also evident, with stellar evolution and collisional mass loss contributing differently across the three mass regimes. In the low-mass model, mass loss has a negligible effect on the overall efficiency, while in the medium- and high-mass models the cumulative mass loss becomes more significant, particularly following the final major collisional events. The time of the last collision, indicated in each panel, marks the end of the rapid growth phase of the MMO within the simulated time span.

4.5 Escapers and mass loss

The formation and subsequent growth of a massive central object are governed by the competition between collisional mass accumulation and several channels of mass loss. In the simulations presented here, mass loss arises through stellar winds, evolutionary phase transitions, collisions accompanied by partial mass ejection, and the escape of stars from the cluster. These processes not only reduce the final mass attained by the most massive object (MMO), but also indirectly regulate its growth by lowering the collision rate, as decreasing stellar masses and gravitational focusing lead to smaller effective collisional cross sections.

The cumulative impact of mass loss on the black hole formation efficiency remains

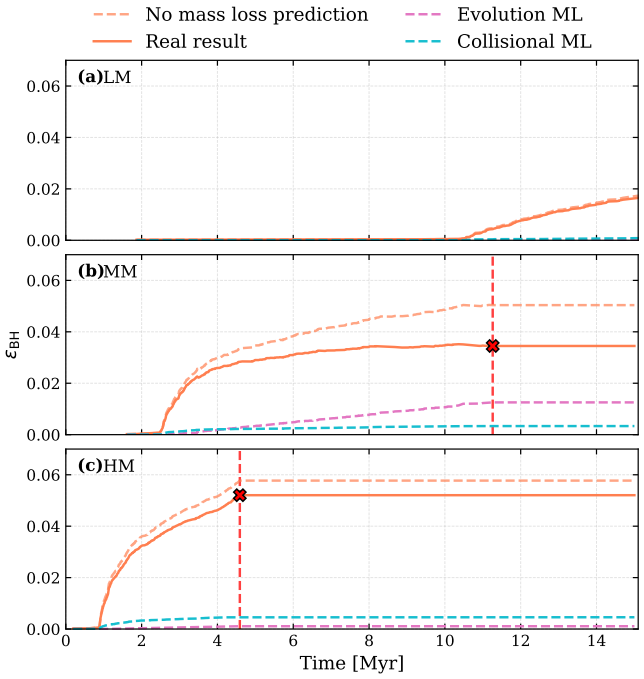

Figure 4.4.1: Time evolution of the black hole formation efficiency, $\epsilon_{\rm BH}$, for non-rotating cluster models with identical global parameters ($N = 10\,\mathrm{k}$, $W_0 = 7$, $\omega_0 = 0.0$) and a total integration time of 15 Myr, but different mean stellar masses. Panels **(a)**, **(b)**, and **(c)** correspond to low-mass (LM; $m_\star = 0.58\,M_\odot$), medium-mass (MM; $m_\star = 10\,M_\odot$), and high-mass (HM; $m_\star = 50\,M_\odot$) models, respectively. The solid orange curve shows the measured black hole formation efficiency associated with the most massive object (MMO). The dashed pink and cyan curves indicate the cumulative mass lost by the MMO due to stellar evolution and collisional processes, respectively. The dashed orange curve represents an estimated efficiency corrected for these mass losses, obtained by adding the collisional and evolutionary mass losses back to the measured $\epsilon_{\rm BH}$. The red cross marks the time of the last collision experienced by the MMO during the simulation. Because the stellar-evolution mass loss is tracked only for the MMO and does not account for mass lost during intermediate evolutionary stages, its total contribution is likely underestimated.

modest compared to the total cluster mass, typically accounting for $\sim$ 0–10% of the final efficiency, depending on the adopted mass model (Figure 4.4.1). Nevertheless, this effect is non-negligible, as it introduces a self-regulating feedback: reduced masses weaken gravitational focusing, which in turn suppresses further collisions and limits additional growth of the central object.

Stellar evolution plays a particularly important role in the massive models. Beyond acting as a continuous source of mass loss, stellar evolution also induces rapid phase transitions. In the high-mass set, most stars evolve into black holes at $t \simeq 5\,\mathrm{Myr}$, leading to a sharp decline in the collision rate. After this epoch, the simulations typically exhibit fewer than $\mathcal{O}(10)$ additional collisions over the remaining integration time, effectively halting the growth of the MMO and fixing the black hole formation efficiency at the value reached at the end of the collisional phase.

Escapers constitute the dominant channel of mass loss at the cluster scale. Although only a fraction of the escaping mass would otherwise have contributed directly to the growth of the MMO, the production of escapers is dynamically significant. Through energy and momentum conservation, interactions that eject stars from the system tend to extract kinetic energy from the remaining bound components, causing them to sink deeper into the cluster potential. As discussed in Section 2.2.3, this process promotes core contraction and increases the central density, thereby facilitating collisional growth despite the net loss of mass.

This dual role of escapers is particularly evident in models with higher initial rotation. These clusters exhibit both larger escaped mass fractions and earlier core contraction, accompanied by enhanced collision rates (Table 4.6.1). In this sense, mass loss through escapers acts not only as a limiting factor on the total available mass, but also as a catalyst for the dynamical conditions required for the formation of a massive central object.

4.6 End-state at 15 Myr

Table 4.6.1, together with Figures 4.5.1 and 4.5.2, provides a compact quantitative and visual summary of the final dynamical outcomes for the low-mass cluster models with smaller particle numbers. Figure 4.5.1 also extends to 25k particles, and in analogy with Figure 4.1.1, highlights the global dependence of stellar

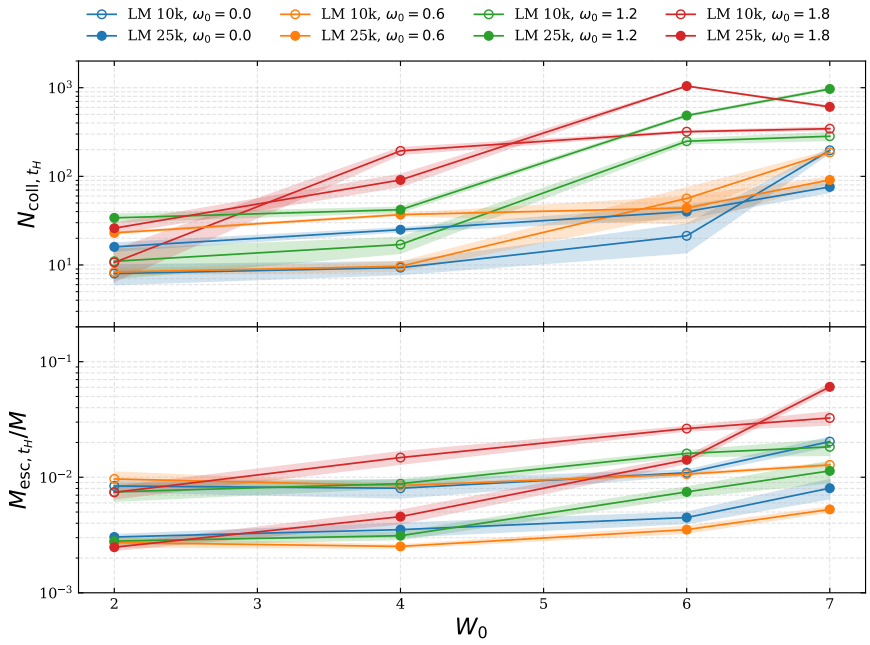

Figure 4.5.1: Total number of stellar collisions, N_{coll,t_H} (top panel), and cumulative escaped mass fraction, $M_{\mathrm{esc},t_H}/M$ (bottom panel), measured at the end of the simulations ($t_H = 15\,\mathrm{Myr}$), as a function of the initial concentration parameter W_0. Results are shown for low-mass cluster models with $N = 10\,\mathrm{k}$ (LM1) and $N = 25\,\mathrm{k}$ (LM2) stars, for all explored values of the initial rotation parameter ω_0. For a fixed concentration, models with larger ω_0 generally exhibit higher collision counts and larger escaped mass fractions in the $N = 10\,\mathrm{k}$ set, consistent with their earlier onset of core contraction. Shaded regions are shown only for the $N = 10\,\mathrm{k}$ models and represent the $\pm 1\sigma$ uncertainty estimated from different random-seed realizations. For the $N = 25\,\mathrm{k}$ models, no uncertainty bands are displayed. The trends in the $N = 25\,\mathrm{k}$ models remain less developed within the simulated time span, as their expected core-collapse timescales exceed the total integration time.

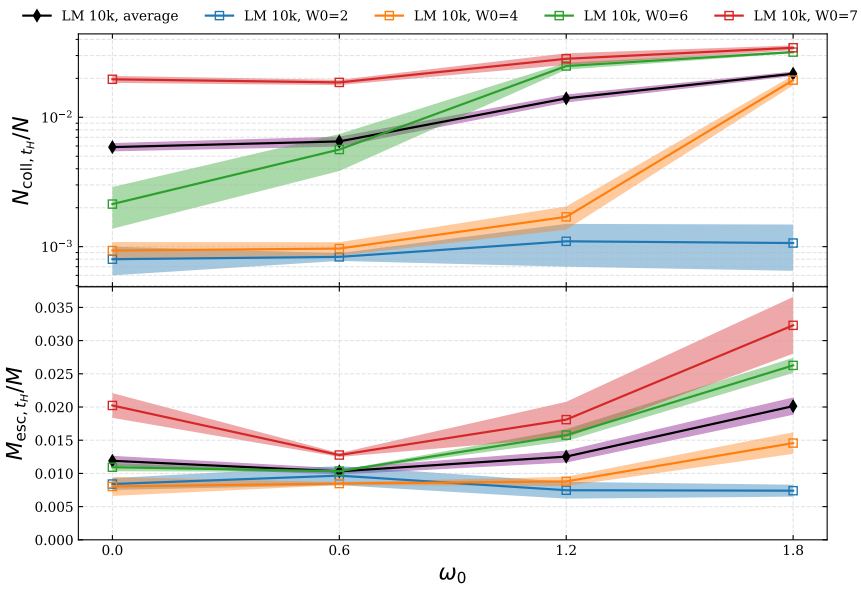

Figure 4.5.2: Total number of stellar collisions, N_{coll,t_H} (top panel), and cumulative escaped mass fraction, $M_{\mathrm{esc},t_H}/M$ (bottom panel), measured at the end of the simulations ($t_H = 15\,\mathrm{Myr}$), as a function of the initial rotation parameter ω_0, for $N = 10\,\mathrm{k}$ models. Individual colored curves correspond to different initial concentration parameters W_0. For each W_0, the black diamond-marked curve shows the mean trend across realizations, while the shaded purple regions indicate the $\pm 1\sigma$ uncertainty associated with different random-seed realizations. These uncertainty bands reflect stochastic variations rather than the dispersion of the models across ω_0. The figure highlights the tendency for more rapidly rotating models to experience earlier core contraction and, consequently, enhanced collisional activity.

Low-mass model (LM1) Number of particles = 10000				
W_0	ω_0	N_{coll,t_H}	$M_{\mathrm{esc},t_H}/M$	$\epsilon_{\mathrm{BH},t_H}$
2	0.0	8.0±2.0	0.00840±0.00089	0
	0.6	8.3±0.6	0.00967±0.00144	0
	1.2	11.0±4.0	0.00747±0.00127	0
	1.8	10.7±4.2	0.00740±0.00090	0
4	0.0	9.3±1.5	0.00803±0.00142	0
	0.6	9.7±1.2	0.00847±0.00023	0
	1.2	17.0±3.5	0.00880±0.00070	0
	1.8	193.7±17.1	0.01457±0.00163	0.0175±0.0021
6	0.0	21.3±7.6	0.01093±0.00060	0
	0.6	56.3±17.9	0.01033±0.00012	0.0018±0.0032
	1.2	249.0±15.4	0.01577±0.00090	0.0227±0.0020
	1.8	319.0±6.1	0.02627±0.00114	0.0294±0.0009
7	0.0	196.7±12.2	0.02023±0.00186	0.0179±0.0013
	0.6	186.0±8.7	0.01277±0.00029	0.0169±0.0012
	1.2	283.3±29.0	0.01810±0.00269	0.0261±0.0030
	1.8	344.7±14.8	0.03230±0.00428	0.0319±0.0012

Table 4.6.1: End-state properties of the low-mass cluster models with $N = 10^4$ particles (LM1), evaluated at $t_H = 15\,\mathrm{Myr}$. For each initial concentration W_0 and rotation parameter ω_0, the table reports the estimated core-collapse timescale t_{cc} for the corresponding non-rotating King model (Quinlan, 1996), the total number of stellar collisions N_{coll}, the cumulative escaped mass fraction $M_{\mathrm{esc}}/M_{\mathrm{tot}}$ and the black hole formation efficiency ϵ_{BH}. The quantities N_{coll} and $M_{\mathrm{esc}}/M_{\mathrm{tot}}$ are measured directly from the N-body simulations at the final output time, and ϵ_{BH} is derived using from the clusters MMO mass.

collisions and mass loss on the initial concentration parameter W_0, while Figure 4.5.2 illustrates the corresponding trends as a function of the initial rotation frequency ω_0.

The core-collapse timescale $t_{\rm cc}$ (Quinlan, 1996), listed for reference in Table 4.6.1, is derived from non-rotating King models with the same initial concentration. As such, it should be regarded only as an approximate indicator of the expected dynamical timescale, since the rotating models considered here experience additional angular-momentum–driven effects. In contrast, the total number of stellar collisions and the escaped mass fraction are direct outcomes of the rotating N-body simulations and therefore encapsulate the combined influence of two-body relaxation, rotation, and close stellar encounters.

For models with low initial concentration, the clusters exhibit modest mass loss through escapers and only a small number of stellar collisions by the end of the simulations at $t_H = 15\,\mathrm{Myr}$. As the concentration increases, both the number of collisions and the escaped mass fraction grow systematically. This behaviour is particularly pronounced for models with $W_0 = 7$, which are characterized by core-collapse timescales shorter than 15 Myr, allowing core contraction and enhanced stellar interactions to develop within the simulated time span.

Excluding the lowest-concentration case ($W_0 = 2$), models with higher initial rotation frequencies generally display larger collision counts and higher escaped mass fractions. This trend reflects the accelerating effect of rotation on core contraction, which promotes earlier onset of high-density conditions and, consequently, more frequent stellar encounters.

Chapter 5

Discussion and Conclusion

5.1 Role of central concentration in early cluster evolution

The influence of the initial central concentration on the onset of collisional activity is illustrated by the collision histograms shown in Figure 5.1.1, which compare non-rotating models ($\omega_0 = 0.0$) with increasing concentration parameters $W_0 = 6, 7, 8$, and 10. Panel **(a)** ($W_0 = 6$) exhibits very weak collisional activity throughout most of the evolution, with only a modest enhancement near the end of the simulation. This behavior reflects the long core-collapse timescale expected for low-concentration systems, which in this case approaches or slightly exceeds the total integration time.

In contrast, panels **(b)**–**(d)** show progressively earlier and more pronounced collision peaks as the concentration increases. For $W_0 = 7, 8$, and 10, the dominant collision peak coincides closely with the core-collapse timescale estimated from the Quinlan formalism, summarized in Table 2.5.1, as indicated by the alignment between the peak collision bin and the reference collapse marker. This systematic correspondence demonstrates that central concentration is the primary parameter regulating the timing of core contraction and the subsequent emergence of a dense, collisionally active core.

The sharpening and temporal advance of the collision peak with increasing W_0 indicate that higher initial concentrations lead to faster central relaxation ($t_{\rm rc}$)

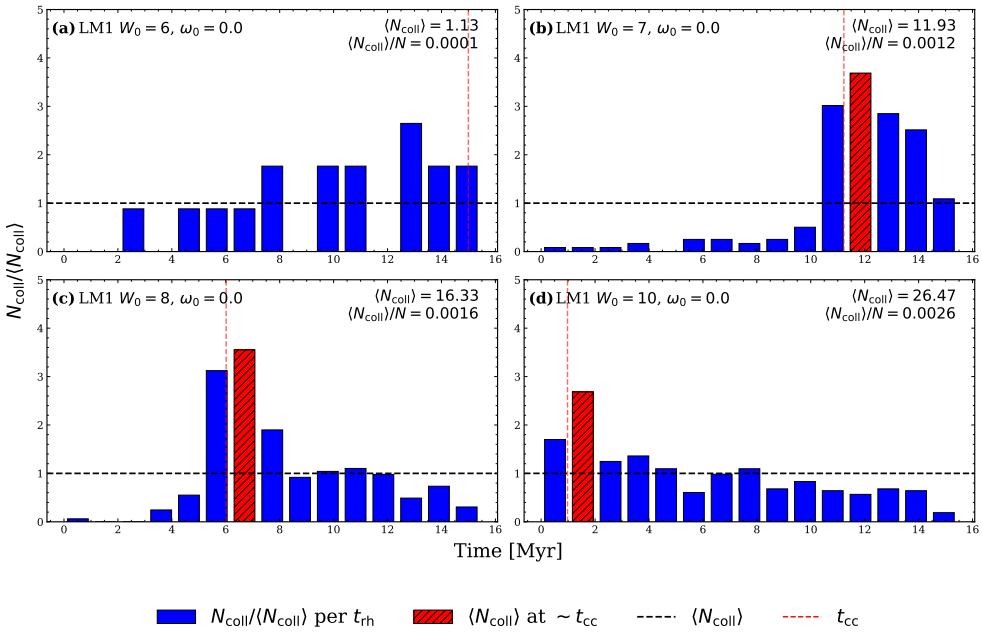

Figure 5.1.1: Normalized collision-rate histograms for non-rotating cluster models ($\omega_0 = 0.0$) with increasing concentration parameters $W_0 = 6, 7, 8$, and 10, shown in panels **(a)**–**(d)**, respectively. The height of each bin represents the number of collisions per bin normalized by the mean collision rate of the corresponding model, while the bin width corresponds to one initial half-mass relaxation time. The vertical marker indicates the estimated core-collapse timescale derived from the Quinlan formalism. Low-concentration models exhibit weak and delayed collisional activity, whereas higher-concentration clusters display progressively earlier and more sharply defined collision peaks that closely coincide with the predicted core-collapse epoch.

and more efficient funneling of stars into the core. Even in the absence of rotation, with only , these models naturally progress toward an early collisional phase once a critical central density is reached, highlighting the dominant role of concentration in setting the baseline dynamical timescale of cluster evolution.

5.2 Impact of rotation on core collapse and collisional activity

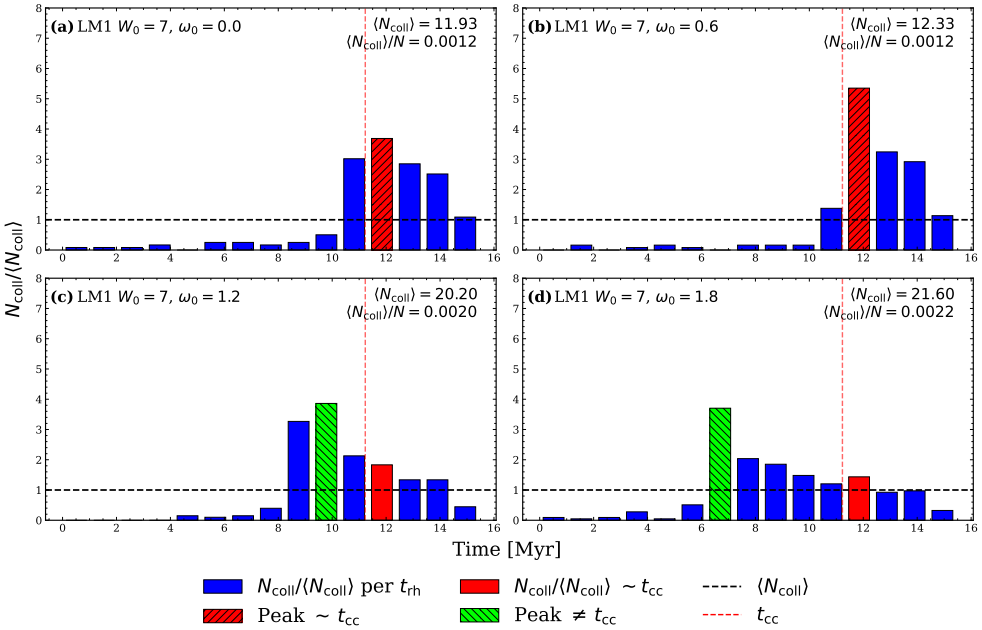

Figure 5.2.1: Normalized collision-rate histograms for cluster models with fixed concentration ($W_0 = 7$) and increasing rotation parameter ω_0. The green dashed bin marks the time interval containing the peak collision rate, while the red bin indicates the interval closest to the Quinlan core-collapse estimate. When the collision peak coincides with the estimated collapse time, the red bin is additionally patterned. As ω_0 increases, the collision peak shifts systematically to earlier times and increasingly precedes the classical core-collapse timescale, indicating that rotational support accelerates central contraction and the onset of collisional activity.

The modulation of core collapse by rotation is examined in Figure 5.2.1, which presents collision histograms for models with fixed concentration ($W_0 = 7$) and increasing rotational support. In these plots, the bin corresponding to the peak collision rate is highlighted in green when it does not coincide with the Quinlan core-collapse estimate, while the bin closest to the estimated collapse time is

marked in red. When the collision peak coincides with the collapse bin, the red bin is additionally patterned, emphasizing their temporal alignment.

For low or moderate rotation, the collision peak remains closely associated with the classical core-collapse timescale, indicating that two-body relaxation remains the dominant driver of central contraction. However, as the rotation parameter ω_0 increases, the peak of collisional activity shifts systematically to earlier times and increasingly precedes the Quinlan estimate. This behavior suggests that rotation accelerates the buildup of central density beyond what is expected from non-rotating models at a fix concentration.

This trend is consistent with the onset of a gravo-gyro instabilityHachisu (1979, 1982), in which angular momentum redistribution enhances inward mass transport and promotes earlier core contraction.

Figure 5.2.2 presents the same set of core diagnostics shown in Figure 4.3.2, but for the corresponding rotating LM1 model with $\omega_0 = 1.8$, allowing for a direct comparison between rotating and non-rotating configurations. At early times, the rotating system exhibits a larger core radius and a higher number of particles within the core, resulting in a lower initial core number density (Table 3.4.1).

This configuration, however, is transient. During the initial phase of the evolution, the rotating core undergoes a rapid structural adjustment, with both r_c and $N(r_c)$ decreasing toward values comparable to those of the non-rotating model. As a consequence, the core number density rises quickly to similar initial levels.

Following this adjustment, the subsequent evolution closely resembles that of the non-rotating case, but with a systematically earlier onset of core contraction and a steeper increase in central density. These results indicate that, although rotation initially inflates the core, it ultimately accelerates the gravothermal evolution by accelerating the onset of core contraction and the formation of a dense, collisionally active central region.

The close temporal correspondence between the contraction of the inner Lagrangian radii and the steepening of the collision curves, as presented in Figures 4.2.2 and 4.2.3 further supports a strong coupling between angular momentum content, core density growth (Figure 5.2.2), and collisional activity. While central concentration remains the primary driver of core collapse, rotation acts as a secondary regulator that advances the timing of the collisional phase and amplifies its early intensity.

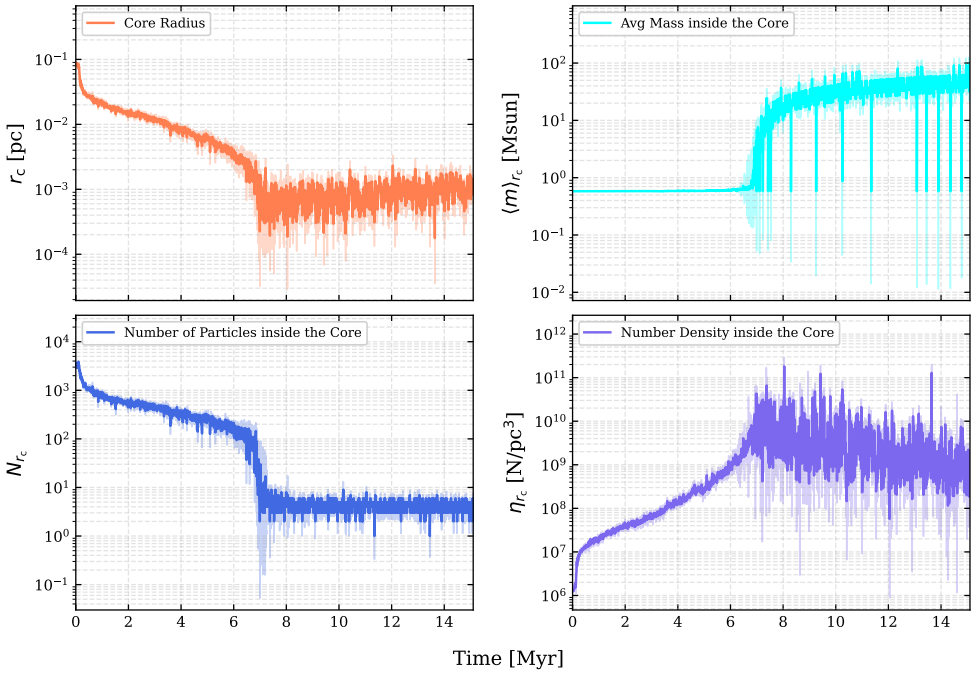

Figure 5.2.2: Time evolution of core structural properties for the low-mass model LM1 ($N = 10\,\mathrm{k}$, $m_\star = 0.58\,M_\odot$, $W_0 = 7$) with initial rotation $\omega_0 = 1.8$. The panels show the core radius r_c, the mean stellar mass enclosed within the core, the number of particles inside r_c, and the corresponding core number density η_{r_c}. Relative to the non-rotating case, the rotating model starts with a larger core and a lower central number density, followed by a rapid early contraction and an earlier rise in core density.

Overall, these results indicate that rotation does not merely modify the morphology of the cluster, but actively reshapes its dynamical evolution by accelerating the transition into a high-density, collision-dominated regime.

5.3 Limitations and numerical considerations

The results presented in this work should be interpreted in light of several numerical and physical limitations inherent to the adopted modeling framework. While the simulations are designed to isolate the roles of central concentration and rotation in driving early cluster evolution, a number of simplifying assumptions necessarily restrict the range of phenomena that can be captured.

Finite-N effects. The particle numbers explored in this study ($N = 10\,\mathrm{k}$, $25\,\mathrm{k}$, and $50\,\mathrm{k}$) remain well below the range of more massive and denser clusters. As a consequence, relaxation-driven processes are artificially accelerated, and stochastic fluctuations associated with small-N dynamics can have a non-negligible impact on the timing and intensity of core collapse and collisional events. This effect is particularly evident in the $N = 25\,\mathrm{k}$ models, where the core-collapse timescale, for concentrations $W_0 < 8$, is comparable to or longer than the total integration time, limiting the ability to fully characterize their late-time behavior. While increasing N improves convergence toward the collisional regime expected in real clusters, the computational cost constrains the accessible parameter space, and residual finite-N effects should be borne in mind when extrapolating the results to larger systems.

Simplified initial conditions and missing physical ingredients. All models neglect primordial binaries, assume a single stellar mass, and evolve in isolation, without an external tidal field or residual gas component. Primordial binaries are known to act as an internal energy source that can delay or even halt core collapse, while a realistic initial mass function would promote early mass segregation and modify both the density structure and collisional cross-sections. Similarly, the absence of an external potential precludes tidal stripping and compressive tidal effects, and the neglect of gas accretion and gas dynamical friction omits potentially important channels for angular momentum redistribution and early cluster contraction. These simplifications imply that the present models should

be regarded as idealized laboratories, aimed at disentangling specific dynamical mechanisms rather than reproducing the full complexity of embedded or tidally limited star clusters.

Collisional Mass-loss Related uncertainties also affect the adopted mass-loss prescriptions. Although mass loss plays a secondary role compared to dynamical ejection and collisional growth in the models presented here, a fully consistent treatment that accounts for the combined influence of rapid stellar rotation, magnetic fields, and detailed chemical evolution remains an active area of development Lombardi et al. (1996); Glebbeek et al. (2009, 2013). As such, the mass-loss rates of very massive stars and collision products may be subject to systematic uncertainties that are closely linked to the current limitations in stellar evolution modeling.

Stellar evolution prescriptions. The treatment of stellar evolution Tout et al. (1997); Hurley et al. (2000, 2002); Heger et al. (2003); Hurley et al. (2013a,b) represents an additional layer of uncertainty on top of the collisional mass loss. The adopted prescriptions are optimized for stars with masses up to $\sim 50\,M_{\odot}$, and extrapolations beyond this range—particularly relevant in dense, collisionally active cores—may not fully capture the true evolution of very massive stars or merger products. In environments where repeated stellar collisions occur, merger remnants may undergo partial rejuvenation, effectively resetting their evolutionary clocks. While this approach provides a convenient parametrization, it may overestimate the lifetimes or long-term stability of collision products in extreme regimes where structural instabilities, rapid rotation, or enhanced mass loss become important. As a result, the growth and longevity of the central massive object should be interpreted as upper limits within the adopted stellar evolution framework.

Scope of applicability. Taken together, these limitations do not undermine the qualitative trends identified in this work—namely the dominant role of central concentration and the secondary, yet significant, influence of rotation on core collapse and collisional activity. However, they do caution against a direct quantitative extrapolation to real young massive clusters. Future studies incorporating higher particle numbers, a realistic mass spectrum, primordial

binaries, and more sophisticated stellar evolution and gas physics will be essential to assess the robustness of these results in more realistic astrophysical environments.

5.4 Summary and conclusion

This work has explored the early evolution of dense stellar clusters in the collisional regime, focusing on the interplay between relaxation-driven core contraction, stellar collisions, and cluster structure. Direct N-body simulations reveal that the contraction of the innermost Lagrangian radii provides a robust indicator of approaching core collapse and closely coincides with enhanced collisional activity. Core diagnostics confirm that the dramatic rise in collision rates is driven primarily by rapid increases in central density rather than by particle accumulation alone.

Initial central concentration emerges as the dominant parameter regulating the pace of evolution, with higher-W_0 clusters undergoing earlier and more pronounced core contraction. Rotation, while initially inflating the core and lowering central density, does not delay collapse; instead, it accelerates the onset of contraction and collisional growth, consistent with efficient angular momentum transport and gravo-gyro–type behavior. Stellar evolution further modulates these processes, promoting early collisional growth in massive models while suppressing late-time collisions through compact-object formation.

Within the adopted numerical framework, the results demonstrate that dense, rotating, and sufficiently concentrated clusters naturally evolve toward conditions favorable for runaway or enhanced stellar collisions and the formation of massive compact objects. While the simplified treatment of collisions, stellar evolution, and the absence of additional physical ingredients impose limitations, the trends identified here provide a coherent physical picture of how cluster structure and rotation regulate the timing and efficiency of collisional core evolution, with direct implications for massive black hole seed formation in dense stellar environments

Bibliography

Aarseth, S. J. (1985). Direct methods for N-body simulations. In Brackbill, J. U. and Cohen, B. I., editors, *Multiple time scales*, pages 377–418.

Aarseth, S. J. (1999). From NBODY1 to NBODY6: The Growth of an Industry. , 111(765):1333–1346.

Aarseth, S. J. (2003). *Gravitational N-Body Simulations*.

Abbott, R. et al. (2020). Properties and Astrophysical Implications of the 150 $M_{\odot}$ Binary Black Hole Merger GW190521. , 900(1):L13.

Ahmad, A. and Cohen, L. (1973). A numerical integration scheme for the N-body gravitational problem. *Journal of Computational Physics*, 12:389–402.

Alister Seguel, P. J., Schleicher, D. R. G., Boekholt, T. C. N., Fellhauer, M., and Klessen, R. S. (2020). Formation of SMBH seeds in Population III star clusters through collisions: the importance of mass loss. , 493(2):2352–2362.

Barack, L. et al. (2019). Black holes, gravitational waves and fundamental physics: a roadmap. *Classical and Quantum Gravity*, 36(14):143001.

Barth, A. J., Martini, P., Nelson, C. H., and Ho, L. C. (2003). Iron Emission in the z = 6.4 Quasar SDSS J114816.64+525150.3. , 594(2):L95–L98.

Bastian, N., Covey, K. R., and Meyer, M. R. (2010). A Universal Stellar Initial Mass Function? A Critical Look at Variations. , 48:339–389.

Binney, J. and Tremaine, S. (2008). *Galactic Dynamics: Second Edition*.

Bromm, V. and Larson, R. B. (2004). The First Stars. , 42(1):79–118.

Carr, B. J. and Hawking, S. W. (1974). Black holes in the early Universe. , 168:399–416.

Chabrier, G. (2003). Galactic Stellar and Substellar Initial Mass Function. , 115(809):763–795.

Chandrasekhar, S. (1943). Stochastic Problems in Physics and Astronomy. *Reviews of Modern Physics*, 15(1):1–89.

Das, A., Schleicher, D. R. G., Leigh, N. W. C., and Boekholt, T. C. N. (2021). Formation of supermassive black hole seeds in nuclear star clusters via gas accretion and runaway collisions. , 503(1):1051–1069.

Einsel, C. and Spurzem, R. (1999). Dynamical evolution of rotating stellar systems - I. Pre-collapse, equal-mass system. , 302(1):81–95.

Escala, A. (2021). Observational Support for Massive Black Hole Formation Driven by Runaway Stellar Collisions in Galactic Nuclei. , 908(1):57.

Escala, A., Zimmermann, L., Valdebenito, S., Vergara, M. C., Schleicher, D. R. G., and Liempi, M. (2025). On the Fate of Little Red Dots. , 995(1):44.

Event Horizon Telescope Collaboration et al. (2019). First M87 Event Horizon Telescope Results. I. The Shadow of the Supermassive Black Hole. , 875(1):L1.

Event Horizon Telescope Collaboration et al. (2022). First Sagittarius A* Event Horizon Telescope Results. I. The Shadow of the Supermassive Black Hole in the Center of the Milky Way. , 930(2):L12.

Fan, X., Strauss, M. A., Schneider, D. P., Gunn, J. E., Lupton, R. H., Becker, R. H., Davis, M., Newman, J. A., Richards, G. T., White, R. L., Anderson, Jr., J. E., Annis, J., Bahcall, N. A., Brunner, R. J., Csabai, I., Hennessy, G. S., Hindsley, R. B., Fukugita, M., Kunszt, P. Z., Ivezić, Ž., Knapp, G. R., McKay, T. A., Munn, J. A., Pier, J. R., Szalay, A. S., and York, D. G. (2001). High-Redshift Quasars Found in Sloan Digital Sky Survey Commissioning Data. IV. Luminosity Function from the Fall Equatorial Stripe Sample. , 121(1):54–65.

Ferrarese, L. and Merritt, D. (2000). A Fundamental Relation between Supermassive Black Holes and Their Host Galaxies. , 539(1):L9–L12.

Gebhardt, K., Bender, R., Bower, G., Dressler, A., Faber, S. M., Filippenko, A. V., Green, R., Grillmair, C., Ho, L. C., Kormendy, J., Lauer, T. R., Magorrian, J., Pinkney, J., Richstone, D., and Tremaine, S. (2000). A Relationship between Nuclear Black Hole Mass and Galaxy Velocity Dispersion. , 539(1):L13–L16.

Genzel, R., Eisenhauer, F., and Gillessen, S. (2010). The Galactic Center massive black hole and nuclear star cluster. *Reviews of Modern Physics*, 82(4):3121–3195.

Georgiev, I. Y., Böker, T., Leigh, N., Lützgendorf, N., and Neumayer, N. (2016). Masses and scaling relations for nuclear star clusters, and their co-existence with central black holes. , 457(2):2122–2138.

Ghez, A. M., Salim, S., Weinberg, N. N., Lu, J. R., Do, T., Dunn, J. K., Matthews, K., Morris, M. R., Yelda, S., Becklin, E. E., Kremenek, T., Milosavljevic, M., and Naiman, J. (2008). Measuring Distance and Properties of the Milky Way's Central Supermassive Black Hole with Stellar Orbits. , 689(2):1044–1062.

Giersz, M. (1998). Monte Carlo simulations of star clusters - I. First Results. , 298(4):1239–1248.

Glebbeek, E., Gaburov, E., de Mink, S. E., Pols, O. R., and Portegies Zwart, S. F. (2009). The evolution of runaway stellar collision products. , 497(1):255–264.

Glebbeek, E., Gaburov, E., Portegies Zwart, S., and Pols, O. R. (2013). Structure and evolution of high-mass stellar mergers. , 434(4):3497–3510.

Hachisu, I. (1979). Gravogyro Catastrophe of Self-Gravitating and Rotating Systems. , 31(3):523–540.

Hachisu, I. (1982). Gravothermal and Gravogyro Catastrophes of Rotating and Self-Gravitating Gaseous Disks. , 34(3):313–335.

Harikane, Y., Zhang, Y., Nakajima, K., Ouchi, M., Isobe, Y., Ono, Y., Hatano, S., Xu, Y., and Umeda, H. (2023). A JWST/NIRSpec First Census of Broad-line AGNs at z = 4-7: Detection of 10 Faint AGNs with M $_{BH}$ 10^6-10^8 M $_\odot$ and Their Host Galaxy Properties. , 959(1):39.

Häring, N. and Rix, H.-W. (2004). On the Black Hole Mass-Bulge Mass Relation. , 604(2):L89–L92.

Hawking, S. (1971). Gravitationally collapsed objects of very low mass. , 152:75.

Hazard, C. and McMahon, R. (1985). New quasars with z = 3.4 and 3.7 and the surface density of very high redshift quasars. , 314(6008):238–240.

Heger, A., Fryer, C. L., Woosley, S. E., Langer, N., and Hartmann, D. H. (2003). How Massive Single Stars End Their Life. , 591(1):288–300.

Herrera-Camus, R., Förster Schreiber, N. M., Vallini, L., Bouwens, R., and Silverman, J. D. (2025). The early universe with jwst and alma. *Nature Astronomy*.

Hurley, J. R., Pols, O. R., and Tout, C. A. (2000). Comprehensive analytic formulae for stellar evolution as a function of mass and metallicity. , 315(3):543–569.

Hurley, J. R., Pols, O. R., and Tout, C. A. (2013a). SSE: Single Star Evolution. Astrophysics Source Code Library, record ascl:1303.015.

Hurley, J. R., Tout, C. A., and Pols, O. R. (2002). Evolution of binary stars and the effect of tides on binary populations. , 329(4):897–928.

Hurley, J. R., Tout, C. A., and Pols, O. R. (2013b). BSE: Binary Star Evolution. Astrophysics Source Code Library, record ascl:1303.014.

Hypki, A. and Giersz, M. (2013). MOCCA code for star cluster simulations - I. Blue stragglers, first results. , 429(2):1221–1243.

Inayoshi, K., Visbal, E., and Haiman, Z. (2020). The Assembly of the First Massive Black Holes. , 58:27–97.

Jiang, L., McGreer, I. D., Fan, X., Strauss, M. A., Bañados, E., Becker, R. H., Bian, F., Farnsworth, K., Shen, Y., Wang, F., Wang, R., Wang, S., White,

R. L., Wu, J., Wu, X.-B., Yang, J., and Yang, Q. (2016). The Final SDSS High-redshift Quasar Sample of 52 Quasars at z>5.7. , 833(2):222.

Kim, E., Einsel, C., Lee, H. M., Spurzem, R., and Lee, M. G. (2002). Dynamical evolution of rotating stellar systems - II. Post-collapse, equal-mass system. , 334(2):310–322.

Kim, E., Lee, H. M., and Spurzem, R. (2004). Dynamical evolution of rotating stellar systems - III. The effect of the mass spectrum. , 351(1):220–236.

King, I. (1962). The structure of star clusters. I. an empirical density law. , 67:471.

King, I. R. (1965). The structure of star clusters. II. Steady-state velocity distributions. , 70:376.

King, I. R. (1966). The structure of star clusters. III. Some simple dynamical models. , 71:64.

Kochanek, C. S. (1992). The Dynamical Evolution of Tidal Capture Binaries. , 385:604.

Kroupa, P. (2008). Initial Conditions for Star Clusters. In Aarseth, S. J., Tout, C. A., and Mardling, R. A., editors, *The Cambridge N-Body Lectures*, volume 760, page 181.

Kroupa, P., Gjergo, E., Jerabkova, T., and Yan, Z. (2024). The initial mass function of stars. *arXiv e-prints*, page arXiv:2410.07311.

Kroupa, P., Tout, C. A., and Gilmore, G. (1993). The Distribution of Low-Mass Stars in the Galactic Disc. , 262:545–587.

Kustaanheimo, P., SCHINZEL, A., DAVENPORT, H., and STIEFEL, E. (1965). Perturbation theory of kepler motion based on spinor regularization. *Journal für die reine und angewandte Mathematik*, 1965(218):204–219.

Lagoute, C. and Longaretti, P.-Y. (1996). Rotating globular clusters. I. Onset of the gravothermal instability. , 308:441–452.

Leigh, N., Böker, T., and Knigge, C. (2012). Nuclear star clusters and the stellar spheroids of their host galaxies. , 424(3):2130–2138.

Leveque, A., Giersz, M., Banerjee, S., Vesperini, E., Hong, J., and Portegies Zwart, S. (2022). A Monte Carlo study of early gas expulsion and evolution of star clusters: new simulations with the MOCCA code in the AMUSE framework. , 514(4):5739–5750.

Lombardi, Jr., J. C., Rasio, F. A., and Shapiro, S. L. (1996). Collisions of Main-Sequence Stars and the Formation of Blue Stragglers in Globular Clusters. , 468:797.

Longaretti, P.-Y. and Lagoute, C. (1996). Rotating globular clusters. II. Relaxation and evaporation. , 308:453–464.

Longaretti, P.-Y. and Lagoute, C. (1997). Rotating globular clusters. III. Evolutionary survey. , 319:839–849.

Lynden-Bell, D. and Eggleton, P. P. (1980). On the consequences of the gravothermal catastrophe. , 191:483–498.

Maiolino, R., Scholtz, J., Curtis-Lake, E., Carniani, S., Baker, W., de Graaff, A., Tacchella, S., Übler, H., D'Eugenio, F., Witstok, J., Curti, M., Arribas, S., Bunker, A. J., Charlot, S., Chevallard, J., Eisenstein, D. J., Egami, E., Ji, Z., Jones, G. C., Lyu, J., Rawle, T., Robertson, B., Rujopakarn, W., Perna, M., Sun, F., Venturi, G., Williams, C. C., and Willott, C. (2024a). JADES: The diverse population of infant black holes at $4 < z < 11$: Merging, tiny, poor, but mighty. , 691:A145.

Maiolino, R., Scholtz, J., Witstok, J., Carniani, S., D'Eugenio, F., de Graaff, A., Übler, H., Tacchella, S., Curtis-Lake, E., Arribas, S., Bunker, A., Charlot, S., Chevallard, J., Curti, M., Looser, T. J., Maseda, M. V., Rawle, T. D., Rodríguez del Pino, B., Willott, C. J., Egami, E., Eisenstein, D. J., Hainline, K. N., Robertson, B., Williams, C. C., Willmer, C. N. A., Baker, W. M., Boyett, K., DeCoursey, C., Fabian, A. C., Helton, J. M., Ji, Z., Jones, G. C., Kumari, N., Laporte, N., Nelson, E. J., Perna, M., Sandles, L., Shivaei, I., and Sun, F. (2024b). A small and vigorous black hole in the early Universe. , 627(8002):59–63.

Makino, J. (1991). Optimal Order and Time-Step Criterion for Aarseth-Type N-Body Integrators. , 369:200.

Makino, J. (1996). Postcollapse Evolution of Globular Clusters. , 471:796.

Mezcua, M. (2017). Observational evidence for intermediate-mass black holes. *International Journal of Modern Physics D*, 26(11):1730021.

Mitchell, P. S., Miller, L., and Boyle, B. J. (1990). Luminous quasars at high redshift. , 244:1–7.

Mowla, L., Iyer, K., Asada, Y., Desprez, G., Tan, V. Y. Y., Martis, N., Sarrouh, G., Strait, V., Abraham, R., Bradač, M., Brammer, G., Muzzin, A., Pacifici, C., Ravindranath, S., Sawicki, M., Willott, C., Estrada-Carpenter, V., Jahan, N., Noirot, G., Matharu, J., Rihtaršič, G., and Zabl, J. (2024). Formation of a low-mass galaxy from star clusters in a 600-million-year-old universe. *Nature*, 636(8042):332–336.

Natarajan, P. and Lynden-Bell, D. (1997). An Analytic Approximation to the Isothermal Sphere. , 286(2):268–270.

Natarajan, P., Pacucci, F., Ricarte, A., Bogdán, Á., Goulding, A. D., and Cappelluti, N. (2024). First Detection of an Overmassive Black Hole Galaxy UHZ1: Evidence for Heavy Black Hole Seed Formation from Direct Collapse. , 960(1):L1.

Neumayer, N., Seth, A., and Böker, T. (2020). Nuclear star clusters. , 28(1):4.

Nguyen, D. D., Seth, A. C., Neumayer, N., Kamann, S., Voggel, K. T., Cappellari, M., Picotti, A., Nguyen, P. M., Böker, T., Debattista, V., Caldwell, N., McDermid, R., Bastian, N., Ahn, C. C., and Pechetti, R. (2018). Nearby Early-type Galactic Nuclei at High Resolution: Dynamical Black Hole and Nuclear Star Cluster Mass Measurements. , 858(2):118.

Nitadori, K. and Aarseth, S. J. (2012). Accelerating NBODY6 with graphics processing units. , 424(1):545–552.

Plummer, H. C. (1911). On the problem of distribution in globular star clusters. , 71:460–470.

Portegies Zwart, S. F., Makino, J., McMillan, S. L. W., and Hut, P. (1999). Star cluster ecology. III. Runaway collisions in young compact star clusters. , 348:117–126.

Portegies Zwart, S. F. and McMillan, S. L. W. (2002). The Runaway Growth of Intermediate-Mass Black Holes in Dense Star Clusters. , 576(2):899–907.

Quinlan, G. D. (1996). The time-scale for core collapse in spherical star clusters. , 1(3):255–270.

Raga, A. C., Rodríguez-Ramírez, J. C., Rodríguez-González, A., Lora, V., and Esquivel, A. (2013). Analytic and numerical calculations of the radial stability of the isothermal sphere. , 49:127–135.

Reines, A. E. and Volonteri, M. (2015). Relations between Central Black Hole Mass and Total Galaxy Stellar Mass in the Local Universe. , 813(2):82.

Reinoso, B., Fellhauer, M., and Véjar, R. (2018). Formation and evolution of substructures in tidal tails: spherical dark matter haloes. , 476(2):1869–1876.

Reinoso, B., Schleicher, D. R. G., Fellhauer, M., Leigh, N. W. C., and Klessen, R. S. (2020). The effects of a background potential in star cluster evolution. A delay in the relaxation time-scale and runaway collision processes. , 639:A92.

Salpeter, E. E. (1955). The Luminosity Function and Stellar Evolution. , 121:161.

Schneider, R., Ferrara, A., Natarajan, P., and Omukai, K. (2002). First Stars, Very Massive Black Holes, and Metals. , 571(1):30–39.

Schödel, R., Ott, T., Genzel, R., Hofmann, R., Lehnert, M., Eckart, A., Mouawad, N., Alexander, T., Reid, M. J., Lenzen, R., Hartung, M., Lacombe, F., Rouan, D., Gendron, E., Rousset, G., Lagrange, A.-M., Brandner, W., Ageorges, N., Lidman, C., Moorwood, A. F. M., Spyromilio, J., Hubin, N., and Menten, K. M. (2002). A star in a 15.2-year orbit around the supermassive black hole at the centre of the Milky Way. , 419(6908):694–696.

Sehlke-Abarca, K. L. K., Escala, A., Schleicher, D. R. G., Reinoso, B., Vergara, M. Z. C., and Solar, P. A. (2023). Formation of very massive objects via collisions of main-sequence Pop. III stars in primordial clusters with a background

potential. *Boletin de la Asociacion Argentina de Astronomia La Plata Argentina*, 64:277–279.

Shu, Q., Pang, X., Flammini Dotti, F., Kouwenhoven, M. B. N., Arca Sedda, M., and Spurzem, R. (2021). The Long-term Evolution of Main-sequence Binaries in DRAGON Simulations. , 253(1):14.

Spitzer, L. (1987). *Dynamical evolution of globular clusters.*

Spurzem, R. (1999). Direct N-body Simulations. *Journal of Computational and Applied Mathematics*, 109:407–432.

Spurzem, R. and Aarseth, S. J. (1996). Direct collisional simulation of 10000 particles past core collapse. , 282:19.

Spurzem, R. and Kamlah, A. (2023). Computational methods for collisional stellar systems. *Living Reviews in Computational Astrophysics*, 9(1):3.

Tout, C. A., Aarseth, S. J., Pols, O. R., and Eggleton, P. P. (1997). Rapid binary star evolution for N-body simulations and population synthesis. , 291(4):732–748.

Trager, S. C., King, I. R., and Djorgovski, S. (1995). Catalogue of Galactic Globular-Cluster Surface-Brightness Profiles. , 109:218.

Tripodi, R., Martis, N., Markov, V., Bradač, M., Di Mascia, F., Cammelli, V., D'Eugenio, F., Willott, C., Curti, M., Bhatt, M., Gallerani, S., Rihtaršič, G., Singh, J., Gaspar, G., Harshan, A., Judež, J., Merida, R. M., Desprez, G., Sawicki, M., Goovaerts, I., Muzzin, A., Noirot, G., Sarrouh, G. T. E., Abraham, R., Asada, Y., Brammer, G., Estrada-Carpenter, V., Felicioni, G., Fujimoto, S., Iyer, K., Mowla, L., and Strait, V. (2025). Extreme properties of a compact and massive accreting black hole host in the first 500 Myr. *Nature Communications*, 16(1):9830.

Turner, E. L. (1991). Quasars and Galaxy Formation. I. The Z $>$ 4 Objects. , 101:5.

Vergara, M. C., Askar, A., Kamlah, A. W. H., Spurzem, R., Flammini Dotti, F., Schleicher, D. R. G., Arca Sedda, M., Hypki, A., Giersz, M., Hurley, J., Berczik, P., Escala, A., Hoyer, N., Neumayer, N., Pang, X., Tanikawa, A., Cen, R., and Naab, T. (2025). Rapid formation of a very massive star $>$50000 $M_\odot$ and subsequently an IMBH from runaway collisions. Direct N-body and Monte Carlo simulations of dense star clusters. *arXiv e-prints*, page arXiv:2505.07491.

Vergara, M. C., Escala, A., Schleicher, D. R. G., and Reinoso, B. (2022). Global instability by runaway collisions in nuclear stellar clusters: Numerical tests of a route for massive black hole formation. *arXiv e-prints*, page arXiv:2209.15066.

Volonteri, M. (2010). Formation of supermassive black holes. , 18(3):279–315.

Volonteri, M., Habouzit, M., and Colpi, M. (2021). The origins of massive black holes. *Nature Reviews Physics*, 3(11):732–743.

Wang, L., Spurzem, R., Aarseth, S., Giersz, M., Askar, A., Berczik, P., Naab, T., Schadow, R., and Kouwenhoven, M. B. N. (2016a). The DRAGON simulations: globular cluster evolution with a million stars. , 458(2):1450–1465.

Wang, L., Spurzem, R., Aarseth, S., Nitadori, K., Berczik, P., Kouwenhoven, M. B. N., and Naab, T. (2015). NBODY6++GPU: ready for the gravitational million-body problem. , 450(4):4070–4080.

Wang, L., Spurzem, R., Aarseth, S., Nitadori, K., Berczik, P., Kouwenhoven, M. B. N., and Naab, T. (2016b). Acceleration of hybrid MPI parallel NBODY6++ for large N-body globular cluster simulations. In Meiron, Y., Li, S., Liu, F. K., and Spurzem, R., editors, *Star Clusters and Black Holes in Galaxies across Cosmic Time*, volume 312 of *IAU Symposium*, pages 260–261.

Willott, C. J., Percival, W. J., McLure, R. J., Crampton, D., Hutchings, J. B., Jarvis, M. J., Sawicki, M., and Simard, L. (2005). Imaging of SDSS z $>$ 6 Quasar Fields: Gravitational Lensing, Companion Galaxies, and the Host Dark Matter Halos. , 626(2):657–665.